Magnetically Actuated Electronics and Robotics for Medical Applications

by

Dakota Edwards

A Thesis Presented in Partial Fulfillment
of the Requirements for the Degree
Master of Science

Approved April 2020 by the
Graduate Supervisory Committee:

Hamidreza Marvi, Chair
Spring Berman
Hyunglae Lee

ARIZONA STATE UNIVERSITY

May 2020

ABSTRACT

Presented in this thesis are two projects that fall under the umbrella of magnetically actuated electronics and robotics for medical applications. First, magnetically actuated tunable soft electronics are discussed in Chapter 2. Wearable and implantable soft electronics are clinically available and commonplace. However, these devices can be taken a step further to improve the lives of their users by adding remote tunability. The four electric units tested were planar inductors, axial inductors, capacitors and resistors. The devices were made of polydimethylsiloxane (PDMS) for flexibility with copper components for conductivity. The units were tuned using magnets and mobile components comprised of iron filings and ferrofluid. The characteristic properties examined for each unit are as follows: inductance and quality factor (Q-factor) for inductors, capacitance and Q-factor for capacitors, and impedance for resistors. There were two groups of tuning tests: quantity effect and position effect of the mobile component. The position of the mobile component had a larger effect on each unit, with 20-23% change in inductance for inductors (from 3.31 μH for planar and 0.44 μH for axial), 12.7% from 2.854 pF for capacitors and 185.3% from 0.353 kΩ for resistors.

Chapter 3 discusses a magnetic needle tracking device with operative assistance from a six degree-of-freedom robotic arm. Traditional needle steering faces many obstacles such as torsional effects, buckling, and small radii of curvature. To improve upon the concept, this project uses permanent magnets in parallel with a tracking system to steer and determine the position and orientation of the needle in real time. The magnet configuration is located at the end effector of the robotic arm. The trajectory of the end effector depends on the needle's path, and vice versa. The distance the needle travels inside the workspace is tracked by a direct current (DC) motor, to which the needle is tethered. Combining this length with the pose of the end effector, the position

and orientation of the needle can be calculated. Simulation of this tracking device has shown the functionality of the system. Testing has been done to confirm that a single magnet pulls the needle through the phantom tissue.

ACKNOWLEDGMENTS

I would like to thank Mahdi Ilami, Alex Petras, Reza Ahmed, Rohan Sharma, Alagarasan Moorthi, and Hamidreza Marvi for all their help with the project.

TABLE OF CONTENTS

Page

LIST OF TABLES

Table Page

LIST OF FIGURES

LIST OF SYMBOLS

Symbol Page

Symbol Page

CHAPTER 1

INTRODUCTION

Magnetic control of wearable or small devices within the body can prove to be beneficial for many traditionally invasive surgeries or to improve the comfort of wearable and implantable devices. It is an attractive idea in healthcare, preventative care, and home-centered medicine. A new class of micro-robotics and in-body medical devices include actuation through magnetism. Two proposed magnetically actuated medical devices will be discussed in this thesis: magnetically actuated tunable soft electronics and a robo-magnetic needle tracking system.

The tunable soft electronics are made of polydimethylsiloxane (PDMS), a stretchable organic silicon, and copper wires or plates for achieving conductive properties. Researchers have been improving the comfort and design of wearable and implantable electronic devices since their invention. With increasing technological advancements in medical devices, tunable soft electronic devices have more of a niche to fill now more than ever. Insertables, medical devices usually located subcutaneously (0.3mm - 15.0mm) (Barbone, Meftah, Markiewicz, & Dellimore, 2019), require electrical components for monitoring vitals or collecting patient data (Duun-Henriksen, et al., 2015), and actuation for the slow release or delivery of therapeutic treatments to patients (Kleiner, 2014).

The following chapter, Magnetically Actuated Tunable Soft Electronics (Ilami M. , et al., 2019), is a publication in ACS Omega and further permissions related to the material excerpted should be directed to the ACS. A link to the paper, including supplementary information, is included in the references. Mahdi Ilami, Reza Ahmed and Dr. Hamidreza Marvi conceived the original idea and designed the study. Ilami and I fabricated the samples and Erskine Thompson set up and calibrated the VNA machine

for the experiments. Ilami and I conducted the experiments. Ilami and Thompson analyzed the results. Ilami and I create the figures and tables. Ilami and Ahmed, Dr. Marvi and I wrote the main manuscript. Saeed Zeinolabedinzadeh supervised characterizing electrical properties and discussing the results. Dr. Marvi supervised the work. All authors reviewed the manuscript.

My personal work on the project entailed collecting the data for each of the four types of devices tested: planar inductors, axial inductors, capacitors and resistors. There were three replicas of each of the four devices, twelve devices to test total. Each device was tested for tunability by adding and changing a mobile component within the device for quantity effects and moving the mobile component within the device for position effects. The mobile component consisted of iron fillings and ferrofluid, which I measured out for each test. The ferrofluid's volume was changed while keeping all others constant and the iron filling's mass was also changed while keeping all others constant for quantity effect experiments; the position of each different mixture was changed for position effect experiments. An axial magnet was used with the axial inductors, and block magnets with the remaining three devices, to test how placement of the magnet with or without the mobile component, affected the properties of each device. I used a Vector Network Analyzer (VNA) for data collection.

The conclusion that I drew from the project was that it is possible to tune these types of soft electronic devices with magnets. While the effects of quantity control can be analyzed, the largest effects lie in position control of the mobile component.

The third chapter of this thesis discusses a tracking system for magnetically steered needles using a permanent magnet located at the end effector of a robotic arm. Needle steering is still a field of research that requires more development before it can become clinically relevant. It requires improved steerability which is hindered due to

torsion effects in the needle shaft, needle buckling, and small radii of curvature. These issues can be resolved by using a magnetic field to steer the needle as opposed to pushing the needle at its base. To properly guide a needle to the desired location it must be precisely tracked. In previous work it was shown that a magnetic field can steer a small magnetic needle through a clear gel by using visual feedback (Ilami, Ahmed, Petras, Beigzadeh, & Marvi, 2020). Ilami et al. used an electromagnetic coil system to produce the magnetic field. Two complications with this system are scalability for clinical applications, and a dependence on accurate visual feedback. This project attempts to incorporate the use of magnetic needle steering with tracking while resolving the previously mentioned obstacles.

CHAPTER 2

MAGNETICALLY ACTUATED TUNABLE SOFT ELECTRONICS

Abstract

Variable electronics are vital in tunable filters, transmitters, and receivers, among other applications. In addition, the ability to remotely tune soft capacitors, resistors, and inductors is important for applications in which the device is not accessible. In this paper, a uniform method of remotely tuning the characteristic properties of soft electronic units (i.e. inductance, capacitance, and resistance) is presented. In this method, magnetically actuated ferrofluid mixed with iron powder is dragged in a soft fluidic channel made of polydimethylsiloxane (PDMS) to tune the electrical properties of the component. The effects of position and quantity of the ferrofluid and iron powder are studied over a range of frequencies, and the changes in inductance, capacitance, resistance, quality factor, and self-resonance frequency are reported accordingly. The position plays a bigger role in changing inductance, capacitance, and resistance. With the proposed design, the inductance can be changed by 20.9% from 3.31 μH for planar inductors and 23% from 0.44 μH for axial inductors. In addition, the capacitance of capacitors and impedance of resistors can be changed by 12.7% from 2.854 pF and 185.3% from 0.353 kΩ, respectively. Furthermore, the changes in the inductance, capacitance, and resistance follow "quasi-linear profiles" with the input during position and quantity effect experiments.

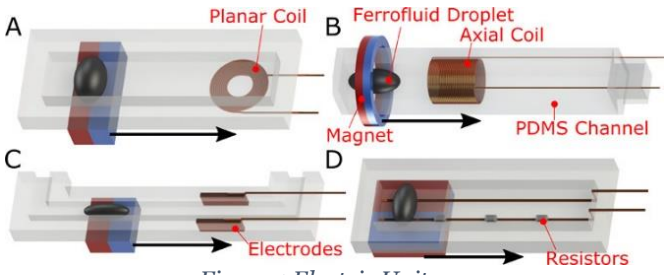

Figure 1 Electric Units

2.1 Introduction

Soft electronics is considered to be a promising replacement for traditional rigid circuits in specialized applications where flexibility, stretchability, and biocompatibility are required. Current commercial integration of soft electronics is limited, but the true measure of this technology's value lies in its potential. Improvements in soft electronics will open doors in several fields. Soft robotics will achieve mobility in highly confined spaces, passively distributing stress to attain robots more robust to their environments (Pang, Lee, & Suh, 2013), (Majidi, 2019), (Yao, Swetha, & Zhu, Nanomaterial-Enabled Wearable Sensors for Healthcare, 2018), (Liu, Pharr, & Salvatore, 2017).

In particular, variable electronic components are vital to applications requiring any type of tuning. Variable resistors are extensively used as control inputs to electronic circuits. Variable inductors can be used for voltage regulation, in tuning the frequencies of inductively coupled power transfer systems and power factor correction over long distances (Wolfle & Hurley, 2003), (James, Boys, & Covic, 2005), (Ito, Yoshihara, Sugawara, Okada, & Masu, 2005). Variable capacitors can also be used for tuning the resonance frequency and capacitive reactance of electrical circuits (Zou, Liu, Schutt-Aine, Chen, & Kang, 2000). In addition, variable components serve a vital purpose in tunable filters, receivers, and transmitters (Buyantuev, Vorobev, Turgaliev, Kholodnyak, & Baskakova, 2018), (Borwick, Stupar, DeNatale, Anderson, & Erlandson, 2003). The addition of these functions will significantly enhance the toolbox of soft electronic device designers.

Through the pursuit of these functionalities, a variety of methods have been developed for achieving soft electronic components and devices. These methods fall into three categories: material innovation, structural design (Wang, Wang, Huang, & Xu, 2018), and mobile liquid conductors. Through material innovation (Yao & Zhu,

Nanomaterial-Enabled Stretchable Conductors: Strategies, Materials and Devices, 2015) (Trung & Lee, 2017), researchers produced conductive composite materials by depositing/embedding conductive nanomaterials onto/within a stretchable substrate (Park, et al., 2018). The resulting composite material is characterized by the conductive properties of the nanomaterial and the mechanical properties of the substrate. Moreover, by using intrinsically stretchable materials such as polydimethylsiloxane (PDMS) doped with nickel, silver, or R-GO microtubes, stretchable electronic devices can be developed (Oh, Lee, & Hong, 2018). These intrinsically stretchable conductive materials can be produced at a low cost because of their simple fabrication process and are characterized by high integrity when stacked in layers. In the structural design category (Wagner & Bauer, 2012), (Kim, et al., 2008), (Rogers, Someya, & Huang, 2010), stretchable interconnects such as waves (Choi, et al., 2007), (Khang, Jiang, Huang, & Rogers, 2006), bridges (Kim, et al., 2008), or meanders of a rigid conductor (Hsu, Gonzalez, Bossuyt, Vanfleteren, & De Wolf, 2011), conductor-filled polymers (Rosset, Niklaus, Dubois, & Shea, 2009), or microfluidic filled with static liquid metals are used to achieve high electrical conductance when bonded to or used in conjunction with stretchable substrates. These stretchable substrates are usually composed of either an elastomeric membrane (Kaltenbrunner, Kettlgruber, Siket, Schwödiauer, & Bauer, 2010), a net made of elastomer (Lanzara, Salowitz, Guo, & Chang, 2010), or a stretched and flattened flex circuit polymer foil (Lewis & Weaver, 2004). For instance, Gray et al. constructed elastomeric electronics by embedding a common helical spring in an elastomer using lithography techniques (Gray, Tien, & Chen, 2004). In addition, using out of plane wavy geometries of solid conductor strands embedded onto a pre-strained elastomer substrate, Choi et al. produced stretchable conductive composites. The effectiveness of

this method depends largely on the design of the waves and meander patterns of the solid conductor (Choi, et al., 2007).

Besides the abovementioned methods, liquid conductors have also been used to develop soft electronic components and devices (Dickey, 2014), (Lu, Wissman, & Majidi, 2015). In this category, development of soft electronics is aided by existing research, concepts, and inventions in the field of microfluidics. Microfluidics is the science of manipulating fluids at the micrometer scale; when a conductive fluid is used, it represents a very viable approach to creating soft, stretchable electronics at a similarly small scale.

The emergence of microfluidics in soft electronics opened a new era, toward using fluids such as liquid metals in electronics. Microfluidic-based electronics is a combination of well-established fields and has evolved largely in the last two decades. Researchers demonstrated that in addition to microfluidic electronic components made of static liquid metal, mobile liquid metals can also be utilized in such components. Jeon et al. used liquid metals with magnetic manipulation to make electrical switches (Jeon, Lee, Chung, & Kim, 2017). In another study, Wang et al. developed a reconfigurable liquid metal antenna driven by electrochemically controlled capillarity (Wang, Trlica, Khan, Dickey, & Adams, 2015).

In addition to liquid metals, ferrofluids are also used for microfluidic electronic applications. Ferrofluid is made of ferromagnetic particles suspended in a carrier fluid. The carrier fluid can be a water or an organic solvent, and ferromagnetic particles are covered with a surfactant to prevent them from clumping (Pamme, 2006). The carrier fluid and surfactant can both be chosen from biocompatible materials, as in commercially available biocompatible ferrofluids. Micro-magnetofluidics is a subfield in microfluidics which studies the use of ferrofluid and other types of magnetic fluids in

microfluidic environments. Micro-magnetofluidics has been successfully used for flow control (Love, et al., 2005), particle sorting and separation (Zeng, Deng, Vedantam, Tzeng, & Xuan, 2013), pumps and valves (Hartshorne, Backhouse, & Lee, 2004), micromixing and assaying (Oh, Jin, Choi, Kim, & Lee, 2007), and droplet formation (Tan, Nguyen, Yobas, & Kang, 2010). Although ferrofluids alone are nonconductive, conductive liquid metal-based ferrofluids have been produced (Mehta, Upadhyay, Dasannacharya, Goyal, & Rao, 1994), (Pant, et al., 2004), (Carle, Bai, Casara, Vanderlick, & Brown, 2017).

Currently, a few tunable microfluidic soft electronic components have been designed and developed. Lazarus et al. devised a stretchable, variable inductor with gallium-filled microfluidic channels in a silicone elastomer and with a ferrofluid core and successfully tested it to 100% strain (Lazarus, Meyer, Bedair, Nochetto, & Kierzewski, 2014). Assadsangabi invented a variable planar inductor using ferrofluid as a core and achieved variability by manipulating the ferrofluid (Assadsangabi, Ali, & Takahata, 2012). In their design, a second planar coil and a permanent magnet lie beneath the inductor in order to manipulate the ferrofluid in a chamber above the inductor. Polcar and Mayer devised a magnetically controllable variable capacitor which uses ferrofluid as the dielectric medium (Polcar & Mayer, 2016). Using a magnetic field to manipulate the ferrofluid dielectric between plates, a variable capacitance is achieved. Furthermore, Liu et al. introduced a variable capacitor made of two stretchable channels filled with liquid metals (Liu, Sun, Hildreth, & Rykaczewski, 2015). Although many of the previously developed microfluidic electronic components are classified as stretchable, flexible, bendable, and/or variable, no research to date presents a full trio of variable electrical components that are tuned via a standardized method. Current variable soft electrical components are variable but most of them require power to be continuously applied in

order to maintain a specific characteristic value. Furthermore, many of these soft variable electronics must be directly adjusted instead of being adjusted remotely.

In this paper, microfluidic soft variable resistors, capacitors, and inductors are presented, all with a standardized tuning method. This method enables remote, magnetic tuning that does not expend power to maintain a tuned characteristic value. The proposed method for tuning the characteristics of the electrical components is based on the effect of a mobile component, which travels through a soft channel. By choosing the mobile component from magnetically responsive materials, it can be actuated using a magnetic field remotely. Having this in mind, ferrofluid is chosen as the mobile component of the proposed stretchable variable electronic units. Additionally, using iron particles as well as mixture of iron particles and ferrofluid is explored as alternatives. This study explores the effects of volume of ferrofluid, mass of iron, and different ratios of their mixture, in different positions inside the channel with and without a magnet on the characteristics of each electronic unit. In particular, a vector network analyzer (VNA) is used to measure the effect of the mobile component on inductance, quality-factor (Q-factor), and self-resonance frequency (SRF) of the inductors, capacitance, Q-factor, and SRF of capacitors, and impedance of the resistors.

2.2 Results and Discussion

In this section, the effect of quantity (cases 1–4; as described in section 2.4.2.1) and position (cases 5–9; as described in section 2.4.2.2) of the mobile components on inductance, Q-factor, and SRF of the inductors; capacitance, Q-factor, and SRF of capacitors; and impedance of the resistors are discussed in detail.

2.2.1 Inductors

Tables 1 and 2 illustrate the results of both position-effect and quantity-effect experiments with the planar and axial inductors, respectively. Among planar inductors, as can be seen in Table 1, case (3) among the quantity-effect and case (7) among the position-effect experiments achieved the broadest tuning range for inductance [2.9% for case (3) and 20.9% for case (7)]. In this table, the inductance is measured at a frequency of 10 MHz.

Table 1 Minimum and Maximum Inductance, Q-Factor, and SRF of Planar Inductors for Different Positions and Quantities of the Mobile Components[a]

case	min(L) ± SEM	max(L) ± SEM	min(Q) ± SEM	max(Q) ± SEM	min(SRF) ± SEM	max(SRF) ± SEM
(1)	4.092 ± 0.069	4.154 ± 0.079	21.7 ± 0.4	23.5 ± 0.6	32.8 ± 1.9	33.0 ± 2.0
(2)	3.320 ± 0.118	3.347 ± 0.117	20.2 ± 1.2	21.4 ± 1.1	36.2 ± 2.3	36.3 ± 2.4
(3)	2.994 ± 0.303	3.081 ± 0.208	16.6 ± 2.2	17.9 ± 1.2	37.0 ± 0.8	37.3 ± 0.6
(4)	3.319 ± 0.069	3.330 ± 0.103	21.6 ± 0.9	22.0 ± 1.4	36.2 ± 2.3	37.5 ± 0.3
(5)	4.025 ± 0.070	4.081 ± 0.058	23.1 ± 0.6	25.1 ± 1.3	32.9 ± 2.0	33.4 ± 2.2
(6)	3.280 ± 0.047	3.753 ± 0.196	18.4 ± 0.4	23.5 ± 2.9	34.3 ± 1.4	35.7 ± 2.0
(7)[b]	**3.309 ± 0.034**	**4.000 ± 0.056**	**19.1 ± 0.7**	**26.6 ± 0.7**	**33.5 ± 2.1**	**35.5 ± 2.3**
(8)	3.327 ± 0.066	3.953 ± 0.026	21.9 ± 1.3	27.1 ± 1.1	34.2 ± 2.1	37.4 ± 0.3
(9)	3.318 ± 0.120	3.990 ± 0.052	21.9 ± 1.2	26.7 ± 0.9	33.7 ± 2.0	36.2 ± 2.3

[a] The inductances are measured at a frequency of 10 MHz and Q-factors at the peak. Minimum, maximum, and the standard error of the mean are calculated based on the data collected from three planar inductors with the same design. The inductances are in μH and the self-resonance frequencies are in MHz. Cases studied in quantity-effect experiments include changing the mass of iron without the magnet being present (case (1)), changing the mass of iron with the magnet being present (case (2)), changing the mass of iron with the magnet and ferrofluid being present (case (3)), and changing the volume of ferrofluid with the magnet being present (case (4)). Cases studied in position-effect experiments include moving iron without the magnet being present (case (5)), iron with the magnet being present (case (6)), a mixture of iron and ferrofluid with the magnet being present (case (7)), ferrofluid with the magnet being present (case (8)), and only the magnet (case (9)).

[b] Case (7) offers the broadest tuning range for inductance among the planar inductors evaluated in this study.

For the axial inductors, case (4) among the quantity-effect and case (7) among the position-effect experiments are the most successful in increasing inductance [increase of 16.33% for case (4) and 23% for case (7)]. From the figures and measurements, it can be concluded that for all the planar and axial inductors explored in this study, moving the mobile component results in more significant changes in inductance than changing its quantity. In Table 2, the inductance is measured at a frequency of 1.5 MHz and the Q-factor at the peak.

The spectral magnitude and spectral phase of the inductors are illustrated in the Supporting Information. As is clear in each phase plot, the phase switches sign at the

SRF. The nonlinear behavior of magnitude at frequencies approaching zero is due to a limit of the VNA.

Table 2 Minimum and Maximum Inductance, Q-Factor, and SRF of Axial Inductors for Different Positions and Quantities of the Mobile Components[a]

case	min(L) ± SEM	max(L) ± SEM	min(Q) ± SEM	max(Q) ± SEM	min(SRF) ± SEM	max(SRF) ± SEM
(1)	0.653 ± 0.007	0.695 ± 0.039	8.4 ± 0.4	9.8 ± 1.0	103.5 ± 4.3	105.5 ± 1.9
(2)	0.427 ± 0.016	0.457 ± 0.009	21.6 ± 5.2	43.1 ± 9.9	122.4 ± 2.5	125.8 ± 2.5
(3)	0.422 ± 0.020	0.438 ± 0.022	27.3 ± 2.0	52.2 ± 11.8	123.5 ± 3.5	125.7 ± 3.9
(4)	0.419 ± 0.018	0.487 ± 0.061	50.3 ± 1.4	58.9 ± 14.9	111.1 ± 4.4	120.5 ± 8.2
(5)	0.517 ± 0.045	0.526 ± 0.049	29.6 ± 8.1	35.1 ± 11.3	115.3 ± 1.7	116.0 ± 1.5
(6)	0.457 ± 0.009	0.510 ± 0.016	21.6 ± 5.2	42.1 ± 8.1	116.6 ± 3.2	122.4 ± 2.5
(7)[b]	**0.438 ± 0.022**	**0.538 ± 0.023**	**27.3 ± 2.0**	**59.8 ± 24.9**	**112.9 ± 0.7**	**123.5 ± 3.5**
(8)	0.443 ± 0.037	0.467 ± 0.028	59.8 ± 13.1	79.3 ± 12.9	114.6 ± 6.4	118.2 ± 10.6
(9)	0.417 ± 0.016	0.490 ± 0.028	58.8 ± 15.3	75.3 ± 6.8	113.1 ± 9.1	121.4 ± 9.6

[a] The inductances are measured at a frequency of 10 MHz and Q-factors at the peak. Minimum, maximum, and the standard error of the mean are calculated based on the data collected from three different axial inductors of cross section 3 mm × 3 mm with the same design. The inductances are in μH and the self-resonance frequencies are in MHz. Cases studied in quantity-effect experiments include changing the mass of iron without the magnet being present (case (1)), changing the mass of iron with the magnet being present (case (2)), changing the mass of iron with the magnet and ferrofluid being present (case (3)), and changing the volume of ferrofluid with the magnet being present (case (4)). Cases studied in position-effect experiments include moving iron without the magnet being present (case (5)), iron with the magnet being present (case (6)), a mixture

of iron and ferrofluid with the magnet being present (case (7)), ferrofluid with the magnet being present (case (8)), and only the magnet (case (9)).

[b] Case (7) offers the broadest tuning range for inductance among the axial inductors evaluated in this study.

The changes in characteristics of the planar and axial inductors under the position and quantity effects are due to the relation of inductance and the magnetic permeability of the material in proximity to the inductor. The increase in permeability is due to the introduction and incremental addition of iron particles and ferrofluid (ferromagnetic materials) to the inductor, both having relative permeability greater than one. In cases (1–4), different concentrations of iron particles and ferrofluid are used. By increasing the amount of iron particles or ferrofluid, the effect on the inductance is increased. In cases (5–8), moving the mobile component to the core of the inductors causes the maximum effect. The differences in the level of effectiveness between cases using iron particles [case (1–3) and (5–7)] and cases using ferrofluid [cases (4) and (8)] are due to the lower concentration of ferrite particles in the ferrofluid. In case (9), bringing the magnet close to the inductor disrupts its magnetic field lines and changes the permeability of space proximal to the inductor, which alters the unit's inductance.

The Q-factor relates the stored energy in the inductor to the dissipated energy, which is typically defined as the ratio of the reactance value to the equivalent resistance value at a given frequency, using a narrow-band approximation approach. The maximum observed change in Q-factor of planar inductors is 8.5% in quantity-effect experiments [case (2)] and 39% in position-effect experiments [case (7)]. In Table 1, the Q-factor is measured at its peak point. Inductance and Q-factor of case (7) are plotted over the frequency range of 0.3–70 MHz in Figure 2a. The effect of position and quantity of the

mobile components on three planar inductors is plotted in Figures S3–S5 in the Supporting Information.

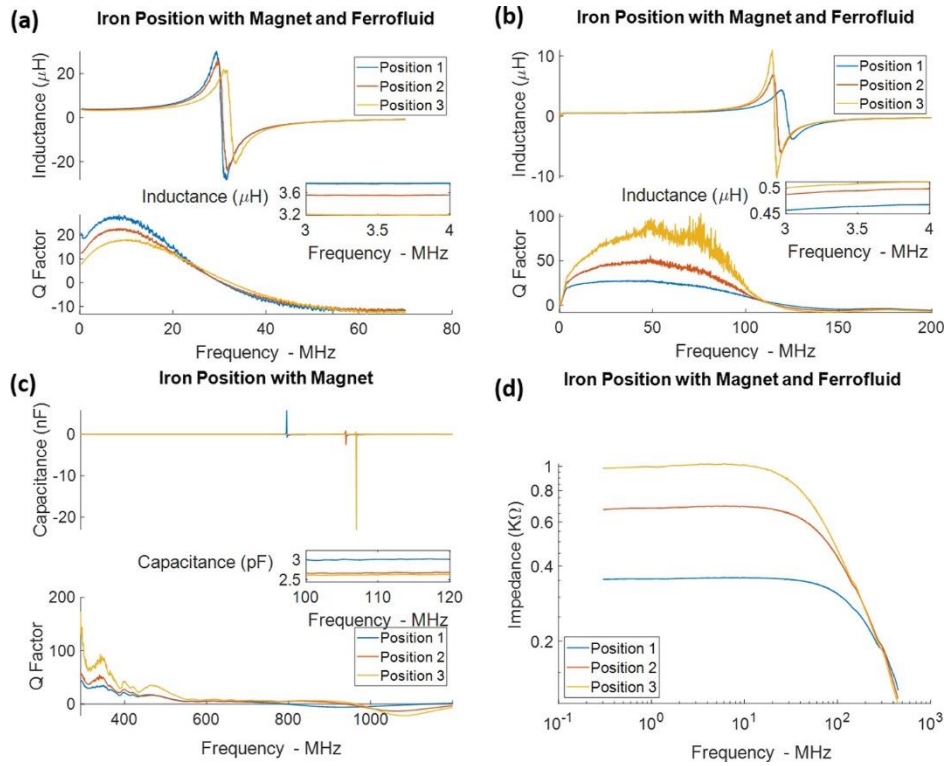

Figure 2 Experiment Plots: Experiments with the most significant change in the tuning range for (a) planar inductor, (b) axial inductor, (c) capacitor, and (d) resistor.

Regarding Q-factor of axial inductors (Table 2), of quantity-effect experiments, the maximum change is 99% in case (2) and of position-effect experiments, the maximum change is 119% in case (7). Inductance and Q-factor of case (7) are plotted over the frequency range of 0.3–200 MHz in Figure 2b. In addition, the effect of position and quantity of the mobile component on three axial inductors is plotted in Figures S6–S8 in the Supporting Information.

It is known that an increase in the inductance results in an increase in stored energy, and thus an increase in Q-factor is expected. Over all experiments, the changes in inductance are greater in cases (5–9); Q-factor similarly experiences larger changes in

these cases, as compared to cases (1–4). However, Q-factor does not linearly change with respect to inductance. Additionally, the presence of a ferrite core can increase the loss and decrease the Q-factor to some extent. As a result of these competing factors, the net change observed in the Q-factor is moderate.

SRF is also affected by changing either the position or quantity of the mobile components. For planar inductors (Table 1), the quantity of the mobile component has a minimal impact on SRF (less than 4%), while its position change results in shifting the SRF more significantly [7.3% for case (9) and 9.4% for case (8)]. For axial inductors (Table 2), case (4) induced the greatest shift in SRF among quantity-effect experiments (8.46%) and among position-effect experiments, case (7) shifts the SRF more significantly (9.36%). SRF of an inductor is inversely proportional to the value of the inductance; therefore, a decrease in SRF is expected from an increase in the inductance value of the component.

2.2.2 Capacitors

The results of both position-effect and quantity-effect experiments for capacitors are detailed in Table 3. In this table, both the capacitance and Q-factor are measured at a frequency of 243 MHz. Results of the experiments conducted on capacitors are plotted in Figures S9–S11 in the Supporting Information. In addition, the spectral magnitude and spectral phase of the capacitors are also plotted in the Supporting Information.

In resemblance to the inductor experiments, it is found that for the capacitors explored in this study, moving the mobile component results in more significant tunability of capacitance than changing its quantity. Of the position-effect experiments, case (6) produces the greatest tuning range of capacitance (increase of 12.7%), and of the quantity-effect experiments, case (2) is the most effective scenario for tuning of

capacitance (increase of 6.5%). Capacitance and Q-factor of case (6) are plotted over the frequency range of 0.3–1200 MHz in Figure 2c.

Table 3 Minimum and Maximum Capacitance, Q-Factor, and SRF of the Capacitors for Different Positions and Quantities of the Mobile Components[a]

case	min(C) ± SEM	max(C) ± SEM	min(Q) ± SEM	max(Q) ± SEM	min(SRF) ± SEM	max(SRF) ± SEM
(1)	2.882 ± 0.138	2.977 ± 0.169	16.3 ± 3.5	19.6 ± 1.7	877.6 ± 21.1	915.5 ± 15.6
(2)	3.086 ± 0.064	3.108 ± 0.011	15.0 ± 0.2	17.6 ± 1.3	854.0 ± 44.3	864.6 ± 37.0
(3)	3.035 ± 0.255	3.082 ± 0.180	24.7 ± 6.5	26.8 ± 7.6	863.8 ± 21.2	888.4 ± 43.5
(4)	2.947 ± 0.195	2.977 ± 0.217	16.1 ± 1.6	20.6 ± 9.1	906.3 ± 33.8	920.4 ± 27.0
(5)	2.797 ± 0.134	2.977 ± 0.169	14.3 ± 2.5	19.6 ± 1.7	877.6 ± 21.1	959.9 ± 12.1
(6)[b]	**2.854 ± 0.174**	**3.218 ± 0.086**	**15.5 ± 1.8**	**23.2 ± 7.7**	**814.8 ± 13.6**	**946.4 ± 26.2**
(7)	2.855 ± 0.201	3.059 ± 0.162	17.9 ± 5.7	21.7 ± 3.8	876.0 ± 17.1	951.5 ± 29.0
(8)	2.950 ± 0.288	2.981 ± 0.213	15.4 ± 4.1	23.6 ± 10.4	904.4 ± 31.2	920.4 ± 57.5
(9)	2.802 ± 0.113	2.930 ± 0.190	13.4 ± 1.5	18.3 ± 4.9	921.2 ± 25.4	955.0 ± 12.0

[a] The capacitances and Q-factors are measured at a frequency of 243 MHz. Minimum, maximum, and the standard error of the mean are calculated based on the data collected from three different capacitors with the same design. The capacitances are in pF and the self-resonance frequencies are in MHz. Cases studied in quantity-effect experiments include changing the mass of iron without the magnet being present (case (1)), changing the mass of iron with the magnet being present (case (2)), changing the mass of iron with the magnet and ferrofluid being present (case (3)), and changing the volume of ferrofluid with the magnet being present (case (4)). Cases studied in position-effect experiments include moving iron without the magnet being present (case (5)), iron with the magnet being present (case (6)), a mixture of iron and ferrofluid with the magnet being present

(case (7)), ferrofluid with the magnet being present (case (8)), and only the magnet (case (9)).

[b] Case (6) offers the broadest tuning range for capacitance among the capacitors evaluated in this study.

In cases (1–3) and (5–7), iron particles conglomerate inside the channels near the magnet resulting in a conductive clustered medium. Considering the thin layer of PDMS between the clustered iron particle medium and each plate, this electronic unit can be conceptualized as two capacitors in series. The total capacitance decreases as the conductive medium grows larger in area. This increase in area is facilitated by either changing the amount of iron particles between the capacitor electrodes through adding more iron particles [cases (1–3)] or moving the mobile component further toward the center of the capacitor's plates [cases (5–7)]. This effect is more significant in the presence of the magnet in cases (2) and (6), as the iron particles under the influence of the magnetic field are more closely forced together between the capacitor plates. This increases the amount of mobile component material between the plates, leaving fewer and smaller air gaps in the conductive cluster in comparison to cases (1) and (5). In cases (3) and (7), using ferrofluid along with iron particles shows counter effects or only moderate changes: the variations in capacitance are smaller in these cases compared to cases (2) and (6), in which ferrofluid is not used. Small effects on capacitance seen in cases (4) and (8) are due to the small dielectric permittivity of ferrofluid which is close to that of air.

Maximum Q-factor change in quantity-effect studies is 36.6% in case (2). Of position-effect experiments, maximum Q-factor change is 53% in case (8). For capacitors, the changes in Q-factor are due to changes in the ratio of stored to dissipated

energy. This relation is formulated in equation 5 showing that through an increase in the capacitance, the Q-factor decreases. In cases (5–7), moving the iron particles between the plates results in a decrease in the capacitance and thus, an increase in the Q-factor. This relation is not linear, as iron particles introduce conduction losses which decrease the Q-factor. In cases (3–4 and 7–8), ferrofluid acts as a dielectric and introduces dielectric loss. Therefore, the net change in the Q-factor is subdued.

With regards to the SRF of capacitors, the results indicate that the change in the amount of the mobile component has only a slight effect on the SRF (less than 9%) while the position of the mobile component causes a more significant shift in the SRF (up to 16%) (Figure S9 in the Supporting Information). SRF of capacitors is inversely proportional to the value of the capacitance. Because the capacitance experiences bigger changes during position-effect experiments, SRF will undergo a more significant shift in these experiments as well.

2.2.3 Resistors

Figure S12a in the Supporting Information shows that the circuit is open when using the mobile component comprised of iron powder without a magnet, as the resistance is too high regardless of the iron mass. Likewise, Figure S12b illustrates that the ferrofluid used in these experiments is not electrically conductive. These results reduce the number of possible experiments which may have an impact on the impedance to four different cases: changing the mass of iron with the magnet being present (case (1)), changing the volume of ferrofluid mixed with iron particles and magnet being present (case (2)), changing the position of iron particles with the magnet (case (3)), and changing the position of iron particles mixed with ferrofluid using a magnet (case (4)).

The results of these experiments are shown in Figures S12c–f, S13, and S14 in the Supporting Information over the frequency range of 0.3–450 MHz.

Figure S12c illustrates that by adding more iron powder under the influence of the magnet (case (1)), the resistance of the mobile component drops. This is due to the alignment of iron particles along the magnetic field direction of two magnets with the configuration shown in Figure 4c, which bridges two wires and connects the circuit. By increasing the amount of iron, the surface area of the mobile component connecting the two wires increases, which leads to a better conductivity. Figure S12d (case (2)) in the Supporting Information shows a slight improvement in the conductivity of the mobile component on adding ferrofluid to it. Adding ferrofluid to iron particles enhances the particles alignment which is likely the reason of slight improvement in conductivity of the mobile component in case (2). Figure S12e (case (3)) illustrates the change in the impedance by moving the mobile component in different positions. This is due to different numbers of resistors being included in the circuit. Finally, Figure S12f (case (4)) shows that adding ferrofluid to the mobile component can improve the result of the position experiment slightly.

Table 4 contains the results of both position-effect and quantity-effect experiments for resistors. The impedance of the resistors is measured at 692 kHz. According to the data, the iron amount (case (1)) has more influence on the conductivity of the mobile component than ferrofluid volume (case (2)). Furthermore, in the position-effect experiments, the resistance of mobile component in case (4) is less than case (3).

Table 4 Minimum and Maximum Impedance for Different Position and Quantity Cases for Resistors[a]

case	min ± SEM	max ± SEM
(1)	0.359 ± 0.007	0.425 ± 0.028
(2)	0.353 ± 0.004	0.354 ± 0.005
(3)	0.359 ± 0.007	1.026 ± 0.006
(4)[b]	**0.353 ± 0.004**	**1.012 ± 0.003**

[a] The impedances are measured at a frequency of 692 kHz. Minimum, maximum, and the standard error of the mean are calculated based on the data collected from three different resistors. The impedances are in kΩ. Cases studied in quantity-effect experiments include changing the mass of iron with the magnet being present (case (1)) and changing the volume of ferrofluid mixed with iron particles and magnet being present (case (2)). Cases studied in position-effect experiments include changing the position of iron particles with the magnet (case (3)) and changing the position of iron particles mixed with ferrofluid using a magnet (case (4)).

[b] Case (4) offers the broadest tuning range for impedance among the resistors evaluated in this study.

2.3 Conclusion

In this paper, we propose a uniform method to add tunability to soft electronic units including inductors, capacitors, and resistors. This method changes the characteristics of soft electronic units using a mobile component moving in a fluidic channel. The effects of both position and quantity of the mobile components on electrical characteristics of each circuit element were fully explored. The results show that the position of the mobile component has more impact on changing the characteristics of the electronic unit. In particular, we show that the inductance of planar inductors can

change up to 20.9% from 3.31 μH by using a mixture of iron and ferrofluid as the mobile component with the magnet being present, the inductance of axial inductors up to 23% from 0.44 μH by utilizing a mixture of iron and ferrofluid as the mobile component with the magnet being present, the capacitance of capacitors up to 12.7% from 2.854 pF under the influence of iron particles as the mobile component with the magnet being present, and impedance of resistors up to 185.3% from 0.353 kΩ by moving the mobile component made of iron particles. In addition, it is shown that the Q-factor of planar inductors changes up to 39% from 19.1, axial inductors up to 119% from 27.3, and capacitors up to 53% from 15.5. The changes in the inductance, capacitance, and resistance follow "quasi-linear profiles" with the input during position and quantity effect experiments. This means that the mobile component can be encapsulated inside the channel and actuated remotely to tune the characteristics of an electronic unit. Moreover, the possibility of using different mixing ratios of iron particles and ferrofluid can provide different tuning ranges and thus different tuning resolutions for the same displacement of the mobile component. This technique can be used for developing tunable electronics with wide tuning ranges (e.g. filters, receivers, and transmitters) for a variety of applications.

2.4 Methods

This study is conducted on resistors, capacitors, and two types of inductors (i.e. one planar inductor and one axial inductor). Three samples of each type are fabricated for data collection. In this section, fabrication processes, experiments, measurements, and calculations are discussed.

2.4.1 Electronic Units Fabrication

All of the units proposed in this study have three main components: a fluidic channel, an electrical component, and a mobile component. Fabrication of each of these components is described in detail in the following.

2.4.1.1 Fluidic Channel

Fluidic channels are designed to contain the mobile component and provide it with a path to move through. These channels are made of PDMS and are fabricated using soft lithography.(46) The PDMS used for channel fabrication is Dow and Corning's Sylgard 184, with the mixing ratio of 1:10.

3D printing is used to fabricate the negative channel patterns. After printing the molds, silicone oil is applied to the surface for ease of demolding. The oil is left on the surface for 1 min, then the excess is lightly blown off, and the mold is put on the hot plate at 90 °C for 10 min. After mixing, the air bubbles trapped in PDMS are released using a vacuum chamber (degassing), and then it is poured into the molds and degassed again. Finally, the molds are placed on a hot plate set to 90 °C for 3 h. Planar coils and resistors (Figure 3a,d) have the same design of channels; first, the channel walls are fabricated out of PDMS. Then, these walls are mounted on a glass slide to complete the channel. Although this can similarly be done by using a layer of PDMS instead of a glass slide, the focus of this study is not on the effect of stretching or twisting the channel. Therefore, glass slides are chosen to eliminate any coupled effects due to unwanted deformation of the channels during the experiments. These channels are 70 mm long, 15 mm wide, and 10 mm deep with the wall thickness of 7 mm on the sides and 4 mm at both ends.

Axial inductors (Figure 3b) are made in two steps: in the first step, a thin wall channel with 0.5 mm thickness is fabricated and copper wire is wound around it; a 3D

printed cubic core is placed inside the channel to reinforce the thin layered PDMS and prevent any deformations during wire winding. In the second step, the channel and the coil go through another PDMS casting process to add 2 mm thickness to the walls of the channel. Using this method, the channel's walls are thick enough to prevent them from deformation during the experiments. In addition, the inductor is close enough to the inner surface of the channel. These channels are 40 mm long with a cross section of 3 mm × 3 mm. The process of fabricating axial inductors is illustrated in the Supporting Information (Figure S24).

The channel walls for the capacitors (Figure 3c) are made with PDMS using soft lithography technique and then attached to glass slides. Designing for a parallel plate capacitor, two slot gaps of 10 mm × 7 mm are considered on each side of the channel with 2.5 mm distance between them. These channels are 1.5 mm wide, 5 mm deep, and 152 mm long (the total loop length).

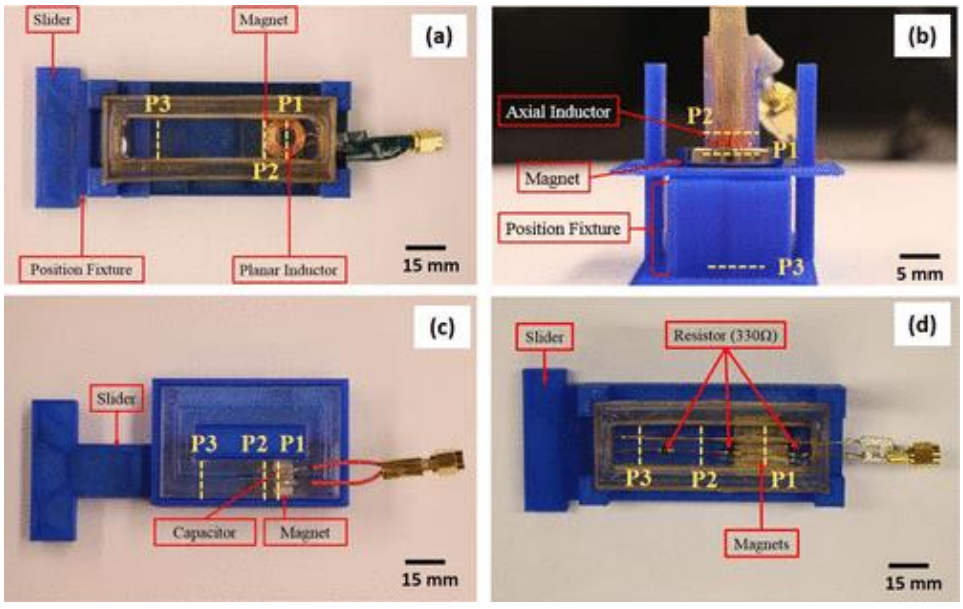

Figure 3 Electric Units: (a) Soft planar inductor placed on the 3D printed mount; a magnet installed on the slider can be stopped at the desired positions using the positioning fixture. (b) Axial inductor, (c) capacitor, and (d) resistor placed on the mount. P1, P2, and P3 indicate different positions of the mobile component during position-effect experiments.

2.4.1.2 Electrical Components

The electrical components used in each unit are made of copper wires and copper plates. Although one can use liquid metals instead of copper to achieve more flexible and stretchable components, that is beyond the scope of this study.

For fabricating the planar inductor units, Mouser Electronics wireless charging coils WE-WPCC are used. We removed 10 rounds of wire from these coils to bring the SRF of the inductor (the frequency at which the parasitic capacitance of an inductor resonates with its inductance) to VNA's frequency range. These coils are attached to the bottom of the glass slides.

For the axial inductor units, copper wire of 28 gauge is wound around the channels over the length of 5 mm. The capacitor units are made of 10 mm × 7 mm copper plates embedded in the channel's slots. The resistor units are made of two parallel wires, each of which connects a series of resistors (Figure 3d). The conductive mobile component moves over both wires and connects them to make a closed circuit. Moving the mobile component back and forth on the wires changes the resistance as different number of resistors can be included in the circuit. A 26 gauge copper wire is used for connecting the series of resistors, and the second wire is 22 gauge. Three 330 Ω surface mounted device (SMD) resistors with 20 mm distance from each other are embedded in the unit. To obtain a continuous change in resistance, one can replace the copper wire and resistors with a high-resistance material.

2.4.1.3 Mobile Component

The mobile component is placed inside the channels and adds variability to each electrical unit. All the mobile components used in this study are magnetically responsive materials; thus, they can be controlled remotely while encapsulated in the channel. In

this study, CMS Magnetics iron powder filings, Educational Innovation FF-310 bulk ferrofluid, and a mixture of both are used as the mobile component. To elaborate on the mixed mobile component, ferrofluid or iron powder (depending on the experiment) is simply combined while inside the channel. Ferrofluid is added using a pipette and the iron powder with a funnel. Further discussion of the mobile component can be found in the following sections and in Table 5. Permanent magnets are used as part of the actuation mechanism of the mobile component inside the channels.

Table 5 Levels of Iron Mass (g) and Ferrofluid Volume (μL) Used in Different Cases[a]

	iron (g)	**magnet + iron (g)**	**magnet + ferrofluid (μL)**	**magnet + iron (g) + ferrofluid (μL)**
planar (L1)	0.123 ± 0.006	0.027 ± 0.002	200	0.068 ± 0.015
planar (L2)	0.163 ± 0.019	0.049 ± 0.004	400	0.119 ± 0.019
planar (L3)[b]	**0.216 ± 0.013**	**0.109 ± 0.015**	**500**	**0.182 ± 0.066**
axial (L1)	0.102 ± 0.008	0.031 ± 0.006	20	0.033 ± 0.001
axial (L2)	0.136 ± 0.004	0.063 ± 0.005	30	0.065 ± 0.001
axial (L3)[b]	**0.171 ± 0.001**	**0.093 ± 0.012**	**40**	**0.096 ± 0.001**
capacitor (L1)	0.063 ± 0.003	0.127 ± 0.001	20	0.028 ± 0.002
capacitor (L2)	0.096 ± 0.003	0.155 ± 0.002	30	0.059 ± 0.001
capacitor (L3)[b]	**0.127 ± 0.001**	**0.186 ± 0.003**	**40**	**0.090 ± 0.002**
resistor (L1)	0.266 ± 0.001	0.116 ± 0.017	100	100
resistor (L2)	0.451 ± 0.001	0.234 ± 0.018	200	200
resistor (L3)[b]	**0.619 ± 0.001**	**0.447 ± 0.013**	**500**	**500**

[a] For magnet + iron + ferrofluid, iron mass is changed for inductors and capacitors and ferrofluid volume is changed for the resistors. The ferrofluid volume is 500 μL for the planar inductor and 40 μL for the axial inductor. In addition, the iron mass used for resistors under this case (magnet + iron + ferrofluid) is 0.447 ± 0.013 g.

[b] Denotes the iron mass and ferrofluid volume used for position-effect studies.

Besides moving the mobile component in the channel, the magnet retains it in place after achieving the desired position. The choice of magnets and their configurations depend on the unit under study (Figure 4). For axial inductors, an axially magnetized ring magnet of NdFeB, Grade N42 with the outer diameter of 19 mm, the inner diameter of 9.5 mm, and thickness of 3.2 mm is used. This magnet slides up and down the inductor to achieve different positions for the mobile component. A block magnet of NdFeB, Grade N42 with dimensions of 19 mm × 9.5 mm × 6.35 mm magnetized through its thickness is used for the planar inductors and capacitors. Two of the same block magnets are used for resistors. The configurations of these magnets with respect to the channels are shown in Figure 4. A 3D printed position fixture is used for consistent positioning of magnets (Figure 3).

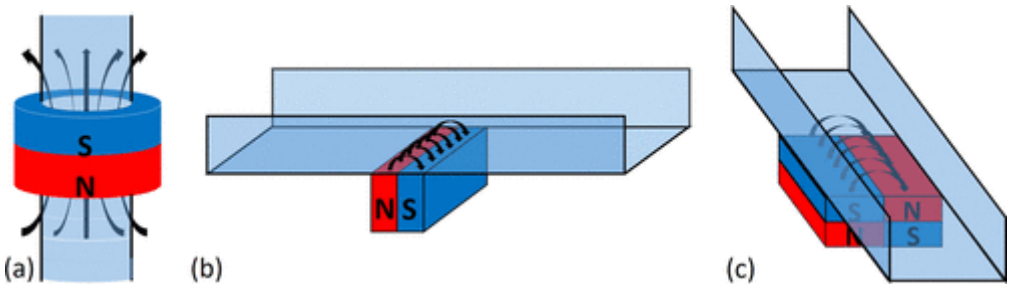

Figure 4 Configuration of Magnets for Each Unit with Respect to the Channels. (a) Axial magnetized ring magnet surrounding a channel is used for axial inductors. (b) For planar inductors and capacitors, a single block magnet is placed such that both poles touch the channel. (c) Two magnet blocks attached to each other are used for the resistors.

2.4.2 Experiments

Experiments are conducted in two different categories to explore the effect of position and quantity of the mobile component on the characteristics of the electrical units. In particular, inductance, capacitance, resistance, Q-factor, and SRF of the units are measured for different positions and quantities of the mobile component.

2.4.2.1 Quantity Effect

For the quantity-effect study, the amount of iron particles and ferrofluid volume are varied. For these measurements, the mobile component is placed at the center of the planar inductors, inside the axial inductors, between the plates for the capacitors, or between the first and the second SMD resistors. The four cases for this study are changing the mass of iron without the magnet being present (case (1)), changing the mass of iron with the magnet being present (case (2)), changing the mass of iron with the magnet and ferrofluid being present (case (3)), and changing the volume of ferrofluid with the magnet being present (case (4)). The amount of ferrofluid and iron used in these experiments are listed in Table 5.

2.4.2.2 Position Effect

For the position-effect study, the mobile component is moved to three different positions. These positions for each of the units are as follows. For planar inductor units, the mobile component is moved to (1) the center of the electrical component (P1), (2) its edge (P2), and (3) 50 mm from the center of it (P3). For axial inductor units, it is moved to (1) inside the electrical component (P1), (2) its edge (P2), and (3) 15 mm from the center of it (P3). For capacitor units, the mobile component is moved to (1) between the plates of the electrical component (P1), (2) its edge (P2), and (3) 30 mm from the center

of those (P3). For resistor units, the three different positions of the mobile component correspond to having one (P1), two (P2), or three (P3) SMD resistors in the circuit. These positions are shown in Figure 3.

The iron mass and ferrofluid volume used for position-effect studies are highlighted in Table 5. The five different cases explored for this study include moving iron without the magnet being present (case (5)), iron with the magnet being present (case (6)), a mixture of iron and ferrofluid with the magnet being present (case (7)), ferrofluid with the magnet being present (case (8)), and only the magnet (case (9)).

2.4.3 Measurements

Measurements are conducted using an Agilent 8712ES VNA (Figure S2 in Supporting Information). The frequency range is kept the same for all three samples of each electronic unit but different between units. The scattering parameter indicating the reflection coefficient on port 1, S_{11}, is measured using one port measurement. The effect of cables and connections are carefully de-embedded using the built-in feature of the instrument and by separate measurements. The intermediate frequency bandwidth for all measurements is set to 250 Hz.

2.4.4 Calculations

Using the S_{11} parameter, the impedance parameter, Z, can be calculated using equation 1.

$$Z = Z_0\left(\frac{1 + S_{11}}{1 - S_{11}}\right) \tag{1}$$

where Z_o is the characteristic impedance of VNA on port 1 (50 Ω in this case).

After obtaining Z-parameters over the frequency (f) range, inductance (L), capacitance (C), and Q-factor for each (Q_L and Q_C, respectively) can be expressed using equations 2–5, respectively.

$$L = \frac{X_L}{\omega} = \frac{X_L}{2\pi f} \tag{2}$$

$$Q_L = \frac{\omega L}{r} = \frac{2\pi f L}{r} \tag{3}$$

$$C = \frac{1}{\omega X_C} = \frac{1}{2\pi f X_C} \tag{4}$$

$$Q_C = \frac{1}{\omega r C} = \frac{1}{2\pi f r C} \tag{5}$$

where X_L and X_C are the reactance's (imaginary part of the Z-parameters) of the inductor and the capacitor, respectively. r is the equivalent series resistance of the component and ω is the resonance frequency (Hiscocks, 2006).

REFERENCES

Assadsangabi, B., Ali, M. M. & Takahata, K., 2012. Ferrofluid-based variable inductor. s.l., s.n., p. 1121–1124.

Borduz, L. & Raj, K., 1987. Low viscosity, electrically conductive ferrofluid composition and method of making and using same. s.l.:Google Patents.

Borwick, R. L. et al., 2003. Variable MEMS capacitors implemented into RF filter systems. IEEE Trans. Microwave Theory Tech., 1, Volume 51, pp. 315-319.

Buyantuev, B. et al., 2018. Electrically controlled variable inductors for applications in tunable filters. s.l., s.n., pp. 487-491.

Carle, F. et al., 2017. Development of magnetic liquid metal suspensions for magnetohydrodynamics. Phys. Rev. Fluids, Volume 2, p. 013301.

Choi, W. M. et al., 2007. Biaxially stretchable wavy silicon nanomembranes. Nano Lett., Volume 7, p. 1655–1663.

Dickey, M. D., 2014. Emerging applications of liquid metals featuring surface oxides. ACS Appl. Mater. Interfaces, Volume 6, p. 18369–18379.

Gray, D. S., Tien, J. & Chen, C. S., 2004. High-Conductivity Elastomeric Electronics. Adv. Mater., Volume 16, pp. 393-397.

Hartshorne, H., Backhouse, C. J. & Lee, W. E., 2004. Ferrofluid-based microchip pump and valve. Sens. Actuators, B, Volume 99, p. 592–600.

Hiscocks, P. D., 2006. Analog Electronic Circuit Design. s.l.:John Wiley & Sons, Incorporated.

Hsu, Y.-Y.et al., 2011. Polyimide-enhanced stretchable interconnects: design, fabrication, and characterization. IEEE Trans. Electron Devices, Volume 58, p. 2680–2688.

Ito, Y. et al., 2005. A 1.3-2.8 GHz Wide Range CMOS LC-VCO Using Variable Inductor. s.l., s.n., pp. 265-268.

James, J., Boys, J. & Covic, G., 2005. A variable inductor based tuning method for ICPT pickups. s.l., s.n., pp. 1142-1146 Vol. 2.

Jeon, J., Lee, J.-B., Chung, S. K. & Kim, D., 2017. On-demand magnetic manipulation of liquid metal in microfluidic channels for electrical switching applications. Lab Chip, Volume 17, p. 128–133.

Kaltenbrunner, M. et al., 2010. Arrays of ultracompliant electrochemical dry gel cells for stretchable electronics. Adv. Mater., Volume 22, p. 2065–2067.

Khang, D.-Y., Jiang, H., Huang, Y. & Rogers, J. A., 2006. A stretchable form of single-crystal silicon for high-performance electronics on rubber substrates. Science, Volume 311, p. 208–212.

Kim, D.-H.et al., 2008. Materials and noncoplanar mesh designs for integrated circuits with linear elastic responses to extreme mechanical deformations. Proc. Natl. Acad. Sci. U. S. A., Volume 105, p. 18675–18680.

Kim, D.-H.et al., 2010. Stretchable, Curvilinear Electronics Based on Inorganic Materials. Adv. Mater., Volume 22, pp. 2108-2124.

Lanzara, G., Salowitz, N., Guo, Z. & Chang, F.-K., 2010. A Spider-Web-Like Highly Expandable Sensor Network for Multifunctional Materials. Adv. Mater., Volume 22, p. 4643–4648.

Lazarus, N. et al., 2014. Multilayer liquid metal stretchable inductors. Smart Mater. Struct., Volume 23, p. 085036.

Lewis, J. S. & Weaver, M. S., 2004. Thin-film permeation-barrier technology for flexible organic light-emitting devices. IEEE J. Sel. Top. Quantum Electron., Volume 10, p. 45–57.

Liu, S., Sun, X., Hildreth, O. J. & Rykaczewski, K., 2015. Design and characterization of a single channel two-liquid capacitor and its application to hyperelastic strain sensing. Lab Chip, Volume 15, p. 1376–1384.

Liu, Y., Pharr, M. & Salvatore, G. A., 2017. Lab-on-Skin: A Review of Flexible and Stretchable Electronics for Wearable Health Monitoring. ACS Nano, Volume 11, pp. 9614-9635.

Love, L. J. et al., 2005. Ferrofluid field induced flow for microfluidic applications. IEEE/ASME Trans. Mechatronics, Volume 10, p. 68–76.

Lu, T., Wissman, J. & Majidi, C., 2015. Soft anisotropic conductors as electric vias for ga-based liquid metal circuits. ACS Appl. Mater. Interfaces, Volume 7, p. 26923–26929.

Majidi, C., 2019. Soft Matter Engineering for Soft Robotics. Adv. Mater. Technol., 12, Volume 4, p. 1800477.

Mehta, R. V. et al., 1994. Magnetic properties of laboratory synthesized magnetic fluid and their temperature dependence. J. Magn. Magn. Mater., Volume 132, p. 153–158.

Oh, D.-W.et al., 2007. A microfluidic chaotic mixer using ferrofluid. J. Micromech. Microeng., Volume 17, p. 2077.

Oh, J. Y., Lee, D. & Hong, S. H., 2018. Ice-Templated Bimodal-Porous Silver Nanowire/PDMS Nanocomposites for Stretchable Conductor. ACS Appl. Mater. Interfaces, Volume 10, p. 21666–21671.

Pamme, N., 2006. Magnetism and microfluidics. Lab Chip, 6(1), pp. 24-38.

Pang, C., Lee, C. & Suh, K.-Y., 2013. Recent advances in flexible sensors for wearable and implantable devices. J. Appl. Polym. Sci., Volume 130, pp. 1429-1441.

Pant, R. et al., 2004. Synthesis and characterization of ferrofluid-conducting polymer composite. Indian J. Eng. Mater. Sci., 8, Volume 11, pp. 267-270.

Park, S. et al., 2018. Silicones for stretchable and durable soft devices: Beyond Sylgard-184. ACS Appl. Mater. Interfaces, Volume 10, p. 11261–11268.

Polcar, P. & Mayer, D., 2016. Magnetic Field Controlled Capacitor. J. Electr. Eng., Volume 67, p. 227.

Rogers, J. A., Someya, T. & Huang, Y., 2010. Materials and Mechanics for Stretchable Electronics. Science, Volume 327, p. 1603–1607.

Rosset, S., Niklaus, M., Dubois, P. & Shea, H. R., 2009. Metal ion implantation for the fabrication of stretchable electrodes on elastomers. Adv. Funct. Mater., Volume 19, p. 470–478.

Tan, S.-H., Nguyen, N.-T., Yobas, L. & Kang, T. G., 2010. Formation and manipulation of ferrofluid droplets at a microfluidic T-junction. J. Micromech. Microeng., Volume 20, p. 045004.

Trung, T. Q. & Lee, N.-E., 2017. Recent Progress on Stretchable Electronic Devices with Intrinsically Stretchable Components. Adv. Mater., Volume 29, p. 1603167.

Wagner, S. & Bauer, S., 2012. Materials for stretchable electronics. MRS Bulletin, 3, Volume 37, p. 207–213.

Wang, C., Wang, C., Huang, Z. & Xu, S., 2018. Materials and Structures toward Soft Electronics. Adv. Mater., 8, Volume 30, p. 1801368.

Wang, M. R. K. M. D. D. M. et al., 2015. A reconfigurable liquid metal antenna driven by electrochemically controlled capillarity. J. Appl. Phys., Volume 117, p. 194901.

Wolfle, W. H. & Hurley, W. G., 2003. Quasi-active power factor correction with a variable inductive filter: theory, design and practice. IEEE Trans. Power Electron., 1, Volume 18, pp. 248-255.

Xia, Y. & Whitesides, G. M., 1998. Soft lithography. Angew. Chem., Int. Ed., Volume 37, p. 550–575.

Yao, S., Swetha, P. & Zhu, Y., 2018. Nanomaterial-Enabled Wearable Sensors for Healthcare. Adv. Healthcare Mater., Volume 7, p. 1700889.

Yao, S. & Zhu, Y., 2015. Nanomaterial-Enabled Stretchable Conductors: Strategies, Materials and Devices. Adv. Mater., Volume 27, pp. 1480-1511.

Zeng, J. et al., 2013. Magnetic separation of particles and cells in ferrofluid flow through a straight microchannel using two offset magnets. J. Magn. Magn. Mater., Volume 346, p. 118–123.

Zou, J. et al., 2000. Development of a wide tuning range MEMS tunable capacitor for wireless communication systems. s.l., s.n., pp. 403-406.

CHAPTER 3

NEEDLE TRACKING FOR PERMANENT MAGNET NEEDLE STEERING

3.1 Introduction

The overall goal of this project is to create a less invasive method for delivering drugs directly to tumors than traditional cancer treatments. More specifically, this project focuses on tracking a small needle being steered inside the body while transporting drugs to a tumor. In order to properly guide this needle to the desired position, its location and orientation must always be known, hence a tracking device is required. The electromagnetic coil system used in Ilami et al. successfully steered the needle with minimal error, but with the caveats of requiring visual feedback and producing too low of forces for clinical applications.

The electromagnetic system used in Ilami et al. is large compared to the workspace and forces it generates. To increase the forces and size of workspace, the size of the system would increase exponentially, making it difficult to be a viable option for clinical use. Permanent magnets, on the other hand, do not increase in size exponentially when compared to the forces they generate. Therefore, permanent magnets have been chosen to steer the needle for this project. The permanent magnet is placed at the end effector of a six degree-of-freedom (DOF) robotic arm. The position and orientation, or pose, of the end effector depends on where the needle needs to go. The needle also has a permanent magnet designed inside of it; therefore, it moves in the direction of the end effector. As part of tracking the needle, it is known that the needle moves some length, L, along the vector between its previous position and the end effector. By vector addition, and not visual feedback, the needle's position and orientation is calculated. The needle has a non-elastic string attached to it which is used to determine the length L that the needle moves by within the workspace. For clinical applications, the string would be a

flexible, non-elastic tube for which drugs travel through to get to the targeted tumor. The string is connected at one end to the needle, and at the other end is wound around a spool that is spinning at a constant rate by a PID-controlled DC motor. This guarantees the length of string being released inside the workspace. To ensure there is no slack within the string, a loadcell is used to constantly measure the string's tension. Figure 5 shows the layout of the tracking system. This method causes very minimal tissue damage as needles are non-invasive and do not require any major incisions.

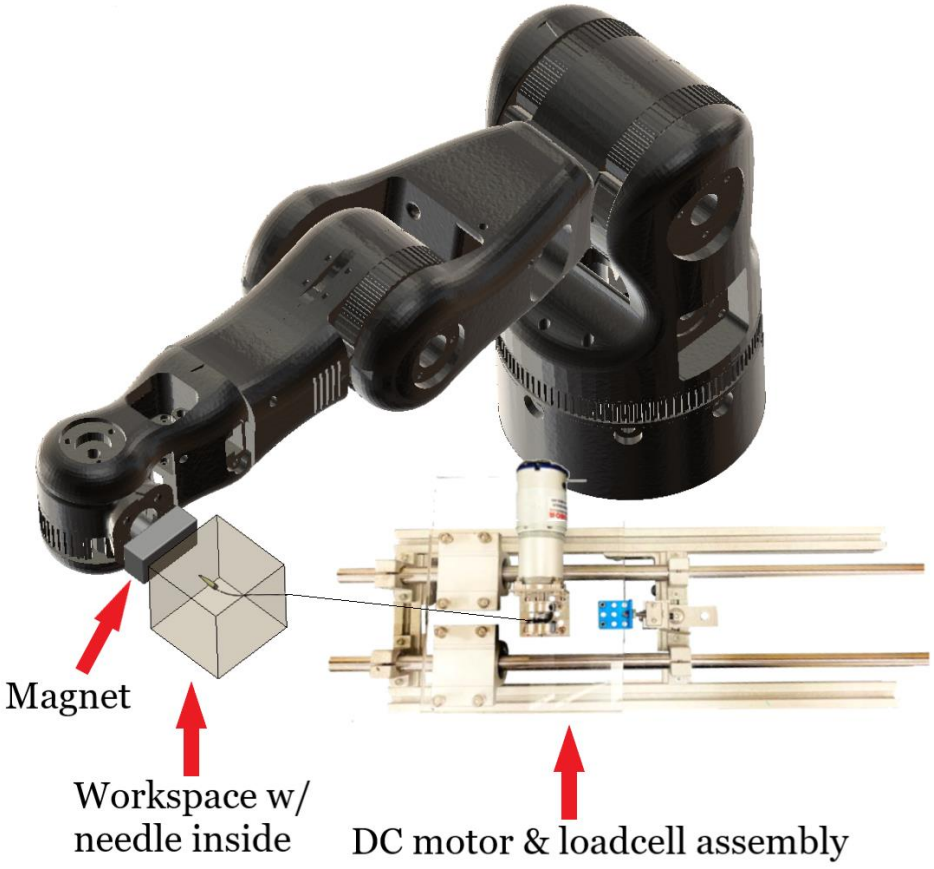

Figure 5 Tracking System Layout/Design

3.1.1 Background

Current clinical methods for treating and removing tumors are deemed invasive for patients: making large surgical incisions to cut out the tumor, or non-targeted drug delivery. Non-targeted drug delivery includes methods such as chemotherapy or immunotherapy; these types of treatments can often cause unintended damage to other healthy cells and organs within the body (Bae & Park, 2011), and may not even successfully rid the body of cancer. Radiation therapy can be a more targeted way to treat cancer but can still have significant damaging effects on nearby healthy cells.

Finding improved non-invasive methods for targeted drug delivery can more accurately eliminate tumors without damaging nearby healthy cells, increase patient healing times, and make cancer treatment a less difficult process. Physically targeted drug delivery is releasing a high concentration of drug to a specific zone without affecting other organs within the body. An example of when targeted drug delivery would prove highly beneficial, or as an only option, include treating glioblastoma, an aggressive tumor within the brain where survival time is 12-18 months. Removal of this type of tumor is practically impossible due to being surrounded by extremely sensitive tissues (Guerreiro & Grotzer, 2018). Physically targeted drug delivery provides a method of avoiding these sensitive obstacles within the brain.

A highly researched area of targeted drug delivery is steering drug-carrying devices inside the body, such as millimeter-scale sized needles or catheters. Current research with catheters involves using a magnetic field to guide the tip of the catheter down already existing channels within the body, while a force is applied to the catheter outside the body to advance the catheter forward. Needle steering is guiding a sharp needle through tissue, creating its own path, to reach a target. If steered properly, it can prove to be beneficial for many medical applications such as convection-enhanced

delivery therapy (CED), or radiofrequency ablation (RFA). CED is a technique utilizing a high-pressure gradient to bypass the blood-brain barrier for targeted drug delivery. RFA uses radio waves to produce an electrical current to heat and ablate tumors. Both treatments require precise guidance to the tumor, achievable by needle steering.

Steering the tip of the needle for conventional needle steering can prove to be difficult, especially for tumors deeper beneath tissue. Conventional needle steering utilizes a long needle inserted into the tissue (Abolhassani, Patel, & Moallem, 2007). To progress the needle through the tissue, forces are applied at the base of the needle, just outside the tissue. At the tip of the needle, interaction forces (created by forces and torques at the base) between the tissue and the asymmetrical tip guide the needle along its path. The minimum radius of curvature for traditional needle steering depends on these interaction forces. Also, the motions at the base do not easily translate to accurate movements at the tip (Reed, Okamura, & Cowan, 2009). Common difficulties that arise from this method of "pushing" the needle are undesirable torsion effects in the needle shaft, needle buckling, and small radii of curvature. Torsional effects arise from frictional forces between the tissue and the needle which creates a deviation between the needle's base and tip rotations, which leads to improper steering. Buckling occurs due to the compression forces: the force at the base of the needle to advance the needle through tissue, and reaction forces exerted at the tip of the needle. These reaction forces can be caused by the non-homogeneity of the tissue such as tissue boundaries or impenetrable objects within the body. Needle buckling is an issue as it can create unintended incisions within the tissue (Reed, et al., 2011) as well as affecting the steerability of the needle; a stiff needle would be required to reduce these buckling effects but the ability to move along a complex path would be compromised.

Applying a pulling force directly at the tip, as opposed to pushing at the base, results in more accurate path tracking and eliminates the issues of torsional effects, buckling, and large radii of curvature. By steering the needle at the tip, the needle does not need to be asymmetrical to navigate, relying only on the pulling forces and not tissue-tip interaction forces. By eliminating the need for an asymmetrical tip, torsional effects are reduced. Also, the radius of curvature no longer depends on the tissue-tip interaction forces and only depends on the length of the rigid needle tip. Furthermore, forces do not need to be applied at the base, therefor buckling is no longer an issue due to the lack of compressive forces. All of this can be achieved by using a short, magnetized needle driven by a magnetic field (Ilami, Ahmed, Petras, Beigzadeh, & Marvi, 2020). In Ilami et al. an eight-coil electromagnetic system (Kummer, et al., 2010) is used to steer a short (0.283 inches) needle made from a permanent magnet. This system gives the needle 5 degrees of freedom (there is no control of the rotation about the needle's main axis).

To test the accuracy of this system they performed two forms of experiments: a radius of curvature test and steering the needle across a boundary between two stiffnesses of gel (gel in the place of tissue). The minimum repeatable radius of curvature that they achieved was 10.2 mm which approaches the length of the needle. For a smaller radius of curvature, it is likely that a shorter needle can be used. This radius of curvature is less than that for conventional needle steering (minimum of 15.5 mm). For the boundary experiments, the maximum deviation of the mean from the path was 2.3 mm when going from soft to stiff gel, with an angle of attack of 45 degrees. The minimum was 0.5 mm going from soft to stiff with an angle of attack of 22.5 degrees. To correct for error along the needle's path, visual feedback is used in a closed loop system.

Difficulties that arise from the electromagnetic system are lack of force and size of the system relative to the workspace. The size of the workspace used in Ilami et al. is 33 mm cubed and a gel that is much softer than real tissue was used to reduce the required forces. This workspace was used for proof of concept but scaling up the system for clinical applications must be considered. The electromagnetic system occupies a relatively large area when compared to the workspace. It also includes a coolant system that wraps cold water around each coil to prevent overheating. To scale this system for clinical applications would require a substantial amount of space in order to generate enough force for steering the needle in a larger workspace.

Another issue that arises from the steering system from Ilami et al. is its dependence on visual feedback to correct for error. The workspace they used was clear and cameras were used to pick up an image of the needle. In real clinical applications this would be difficult since human tissue is opaque and visual feedback provided by current clinical technology may be expensive or have low resolutions when tracking an object as small as a needle. Current clinical methods of tracking include X-ray, Ultrasound and MRI (Cabreros, Jimenez, Greer, Adebar, & Okamura, 2015). It is still, however, necessary to have an improved method for tracking the needle for in-lab and potential clinical use. It has been noted in previous research that while some visual systems may retrieve the position of the needle, they fail to determine the orientation of the needle tip due to noise and needle size (Benam, Talebi, & Khosravi, 2019). Not knowing the tip orientation can be consequential for needle steering. If the needle is pulled in a direction not aligned with its orientation, tissue damage can occur and steerability of the needle compromised. Benam et al. achieved bounded error on simulations for tracking the position and orientation of the needle tip using a high-gain full observer for traditional needle steering. The proposed design in this chapter is for

non-traditional needle steering using permanent magnets and may potentially provide more accuracy for needle-tip tracking.

3.2 Methods and Materials

3.2.1 Needle Fabrication

The primary goals of needle fabrication are sleekness and small size. The overall design of the needle includes one cylindrical permanent magnet (1/16" dia. X 1/4" thick), FDA-Bond 2 epoxy, a severed tip of a 20 G BD PrecisionGlide™ needle, and Kevlar string (Figure 6).

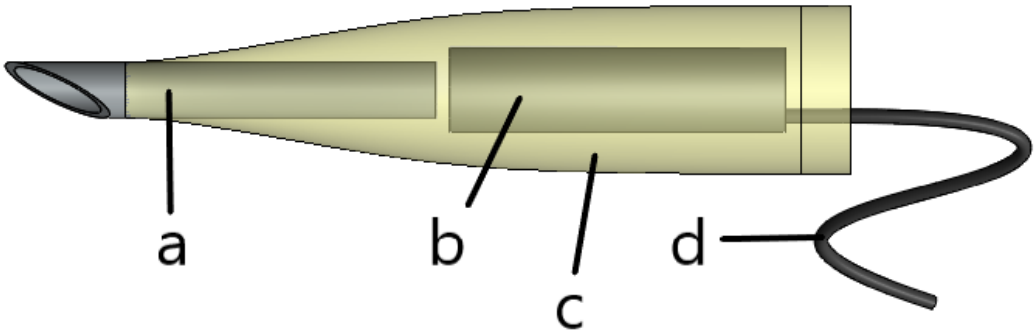

Figure 6 Needle Design: (a) Needle tip (b) Magnet (c) Epoxy (d) Kevlar

The Kevlar string was first attached to the magnet using a dab of epoxy and was then set aside to dry. The needle was made using two halves of a 3D printed mold (Figure 7). A thin layer of car wax was used to cover the mold to help the needle be released. Once the wax was dry, epoxy was used to coat both halves of the mold. The needle and magnet/Kevlar were placed in one half, and then both halves were pressed together and placed in a vice-grip to dry overnight. Once dry, the halves were separated very carefully, and the needle removed, using a blade and rubber mallet.

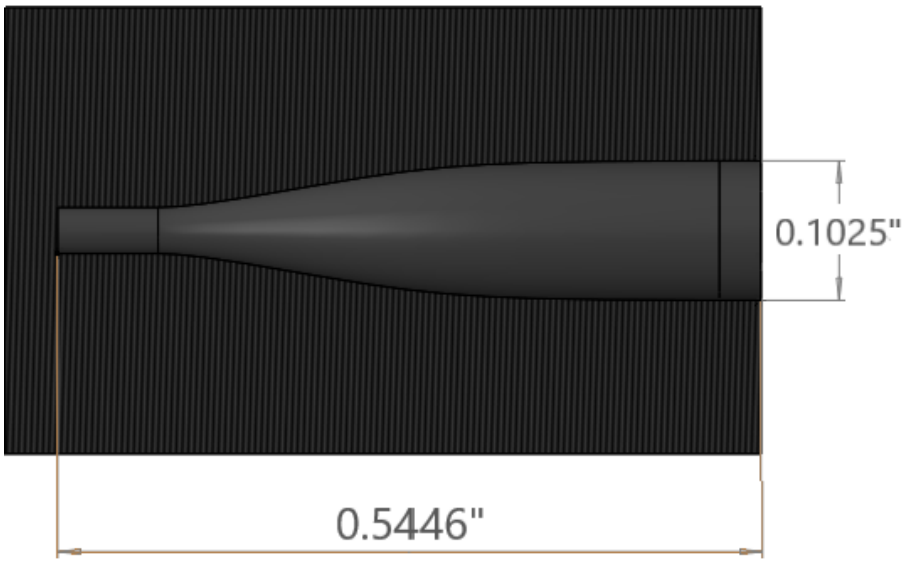

Figure 7 Needle Mold

3.2.2 Loadcell and DC Motor Track

Kevlar string was wrapped around a spindle that was attached to a DC motor. While the motor spins at a constant rate, the Kevlar is also unwound at a constant rate. The DC motor used in this assembly was a 12 RPM Robotzone Planetary gear motor with encoders, alongside a SyRen 25 V1.10 motor driver. A high-torque motor was chosen to account for potentially high tension in the Kevlar string due to the strength of the magnetic field. Having feedback from the encoders was necessary for ensuring the amount of Kevlar that was released. The DC motor was controlled via a PID controller in Arduino.

While the needle was being pulled through the workspace by the magnetic field, tension was being applied to the Kevlar string. If in non-homogenous types of tissue, the needle may run into an obstacle, creating slack within the string. If slack were to occur, the tracking system would be unreliable without a fail-safe mechanism. The tracking system computes L from the equal relationship between the amount of string released

from the DC motor and the amount of string that enters the workspace. When there is slack, that means the DC motor is releasing more string than what is entering the workspace and the length L calculation would be false. To account for this common non-homogeneity of tissues, a loadcell was used to constantly measure forces within the string. The DC motor was placed on a frictionless track that was attached to the stable loadcell. When slack occurred, the pulling forces on the loadcell decreased, signaling that there was slack within the tracking system. When slack was detected, the program would pause and the DC motor reversed direction until there was once again tension within the string. The DC motor was mounted onto a plexiglass plate (Figure 8) which was also mounted to shaft-sliding linear bushings. These bushings slid without friction along two rods so that frictional forces would not affect the loadcell readings of tension within the string. Also attached to the plexiglass was the load pin from a Transducer Techniques loadcell. The forces read by the loadcell went through a calibrated Transducer Techniques signal conditioner before being sent to the tracking program.

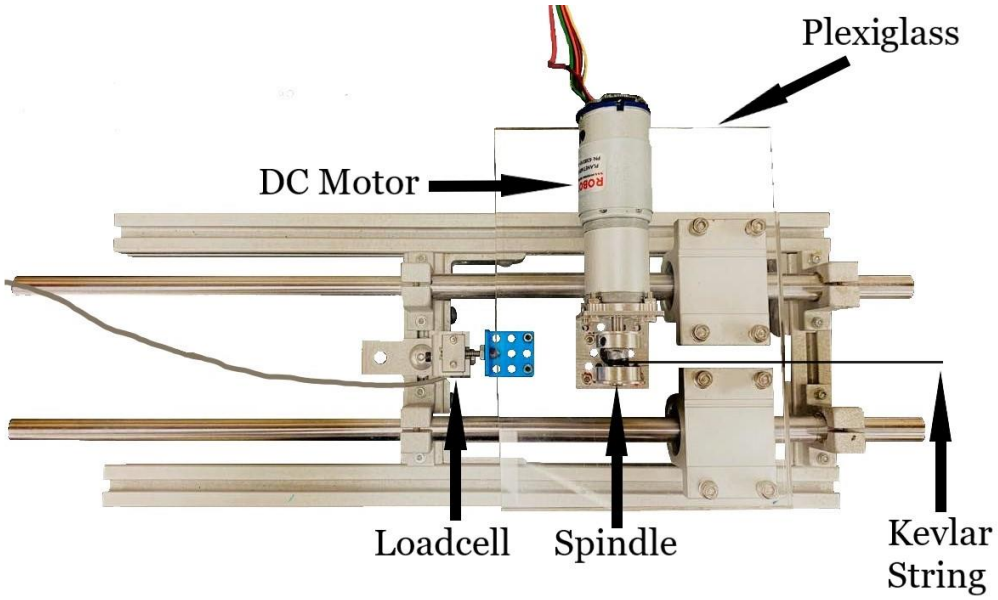

Figure 8 DC Motor and Loadcell Assembly

3.2.3 Gel and Workspace

The gel that was used as the phantom tissue has a low stiffness (2.70 kPa) when compared to real tissue. Due to this project being a proof-of-concept, it was not necessary to have a stiffer gel. Having a stiffer gel would require more puncturing force from the needle which would require a stronger magnet. This would add unnecessary costs when a smaller magnet can prove the concept just as well. The gel is comprised of 1.6 g of agar gelling powder per 100 mL of distilled water.

The size of the workspace is a 2.5 x 2.5 x 2.5-inch cube. This size was chosen while considering the required distance between the needle and end effector. If the distance between the two permanent magnets was too large, there would not be enough force to pull the needle.

3.2.4 Robotic Arm and End Effector Magnet

For this project, a RBX1 (Remix): 3D Printed 6 Axis Robot Arm Beta Kit from Roboteurs was used. It included these essential items:

- 7 Stepper motors from NEMA23 to NEMA14
- A Servo motor for the gripper
- Timing Belts and Pulleys (5 belts and 5 pulleys)
- Shafts and Couplers for internal mechanisms
- All joint bearings and belt tensioner bearings
- All fasteners and basic tools needed for assembly
- Wiring (pre-assembled with the motors)
- SlushEngine Model D motor controller
- Power Supply
- Bootable SD card with Raspberry Pi and all software required

- 3D CAD files for each link

Once the arm was received, each CAD file was 3D printed in ABS. The arm was assembled as shown in Roboteur's tutorial videos. It was soon discovered that the SlushEngine was not substantial and was replaced with seven separate motor drivers: two DM420Y drivers for the shoulder joint and five DM542T drivers for the remaining joints (Figure 9). An Arduino Mega was also used in place of the Raspberry Pi. A new code was written for the robotic arm in Arduino, which can be found in the Appendix.

Denavit-Hartenberg parameters (DH parameters) are a way of defining a series of rigid links by attaching reference frames on each link. There are four parameters: a defines the length of the common normal between consecutive frames; d defines the length of the intersection of the common normal, along the previous frame's z-axis; α is the angle about the common normal to align the previous z-axis with the following z-axis; and θ is the rotation about the z-axis. The DH parameters for the robotic arm are found in Table 6.

Table 6 DH Parameters

Link	**a**	**α**	**d**	**θ**
1	0	π/2	6.66	q_1
2	8.7	0	0	q_2
3	0	π/2	0	q_3
4	0	-π/2	9.06	q_4
5	0	π/2	0	q_5
6	0	0	3.78	q_6

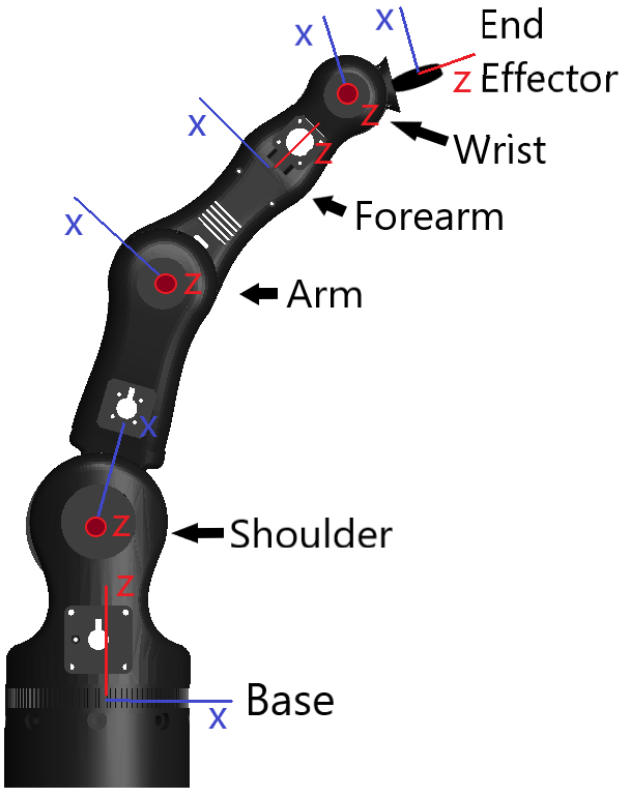

Figure 9 Robotic Arm with Reference Frames and Labels

These DH parameters are necessary to perform inverse and forward kinematics which are needed to calculate the needle position. Inverse kinematics is used when a desired end effector pose is given, and each joint angle needs to be computed. Forward kinematics is when the joint angles are known, and the end-effector pose needs to be calculated. As previously mentioned, the desired position of the end effector was calculated based off where the needle needed to go. Inverse kinematics was performed for every needle step, to calculate each joint angle. These joint angles are then sent from Simulink to Arduino.

The magnet placed at the end effector for attracting the needle is a N50 2”x1”x3/4” rare earth block magnet. There were several other magnet configurations that

were simulated, each consisting of more than one magnet. Other configurations were tested because it was desired to have the robot move the needle by hovering above the needle instead of pulling the needle from the front. An example of a configuration simulated as part of this project is shown in Figure 10. In the end, a single magnet was selected to pull the needle due to project time constraints, as it was challenging to find the right configuration to exert the required forces and torques on the needle. It would still be ideal to have a different magnet configuration for clinical applications. This topic will be discussed further in the Future Work section.

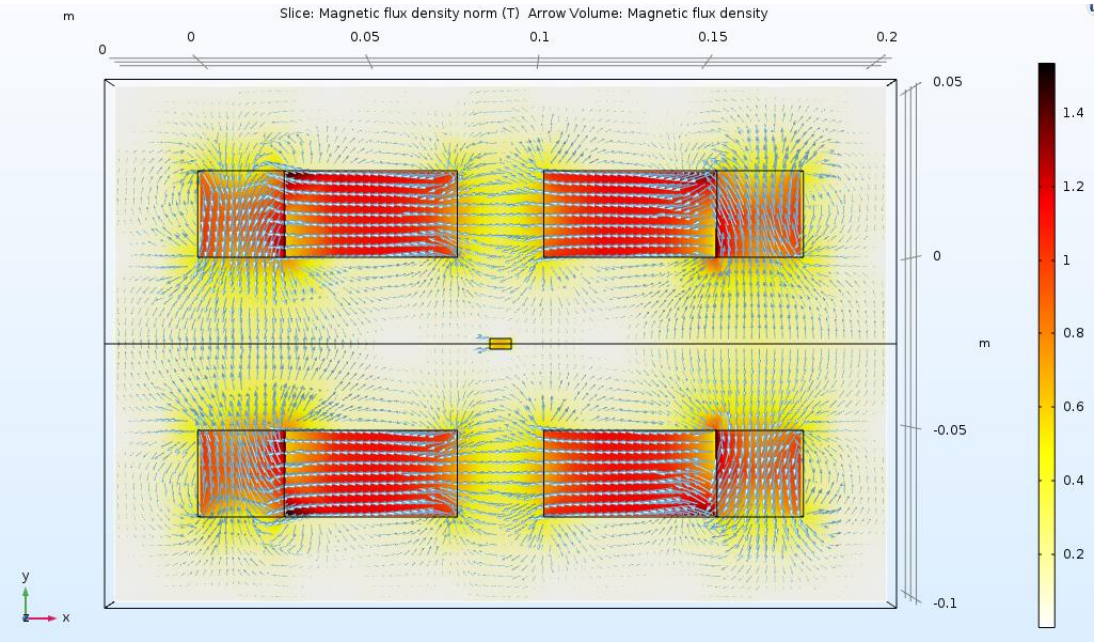

Figure 10 Alternative Magnet Configuration in COMSOL: Needle magnet is centered

3.2.5 MATLAB and Simulink

Two toolboxes were used to define and plot the robotic arm: The Robotics System Toolbox and the Peter Corke Toolbox. The Peter Corke toolbox was only used for plotting the arm because of its simplicity. Using the Robotics System Toolbox, a rigid body tree was defined using the DH parameters and saved to the workspace. This rigid body tree

also incorporates the joint limits. For Peter Corke, a serial link was used. The code for this can be found in the Appendix.

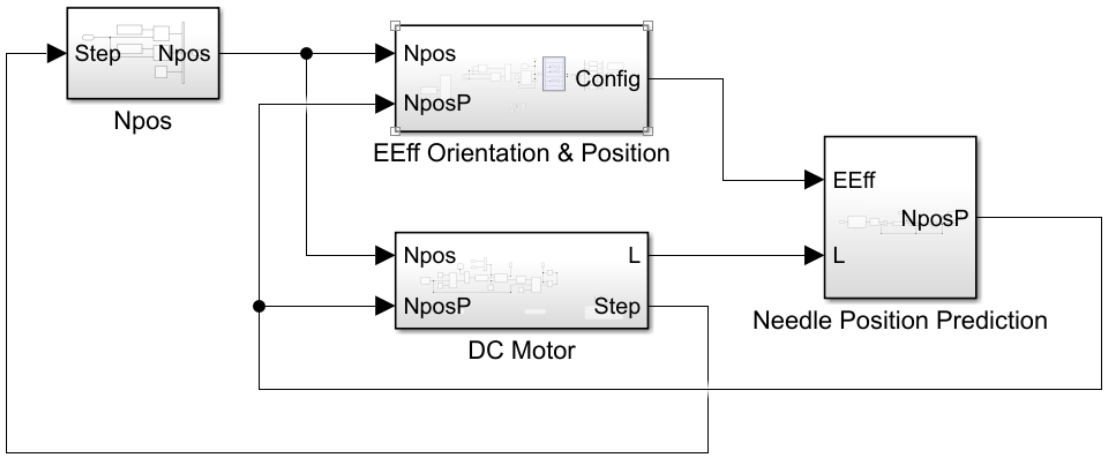

Figure 11 Overall Simulink Layout of Tracking System

The input to the system, Npos, consists of several tightly spaced discretized points along the needle's desired path. Npos is a matrix of size [3xN] where N is the number of points. The output, NposP, is the predicted position of the needle in real time. The first subsystem of the tracker shown in Figure 11 is called Npos and is shown in Figure 12. Here the program steps through Npos from the workspace, one position at a time.

The subsystem labeled EEff Orientation & Position calculates the required end effector pose based off the next desired needle position and the previous/predicted needle position. The output is a [6x1] vector consisting of each joints' angles. This subsystem is shown in Figure 14. The subsystem EEff Position, where the end effector's position is calculated, is shown in Figure 15. The magnet/end effector's z-axis needs to be aligned with the path that the needle travels along, therefore it is aligned with the normal

vector between the needle's previous and desired positions. The maximum distance between the needle and the magnet, to generate the required force to move the needle, is 2.5 inches. The pulling force at this distance is 0.23 N, which is enough to move through the selected gel. This vector is then added to the needle's previous position the get the magnet's coordinates in the global frame. Figure 13 shows a visual representation of the dependence between the needle and magnet's positions.

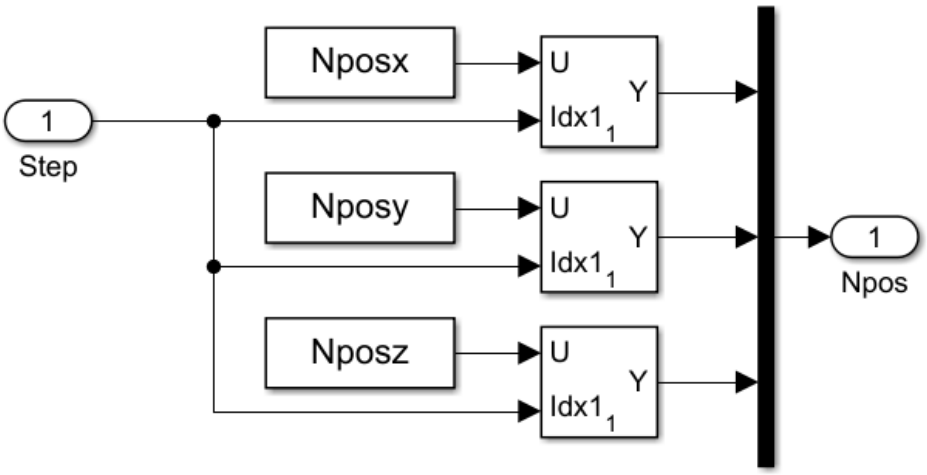

Figure 12 Npos Subassembly

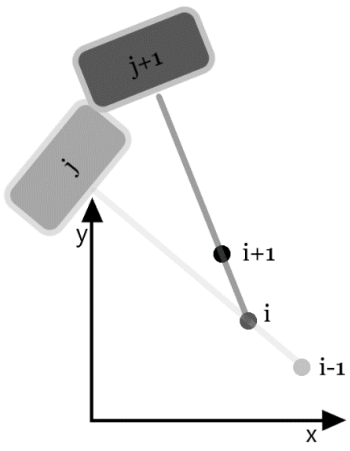

Figure 13 Magnet and Needle Relationship

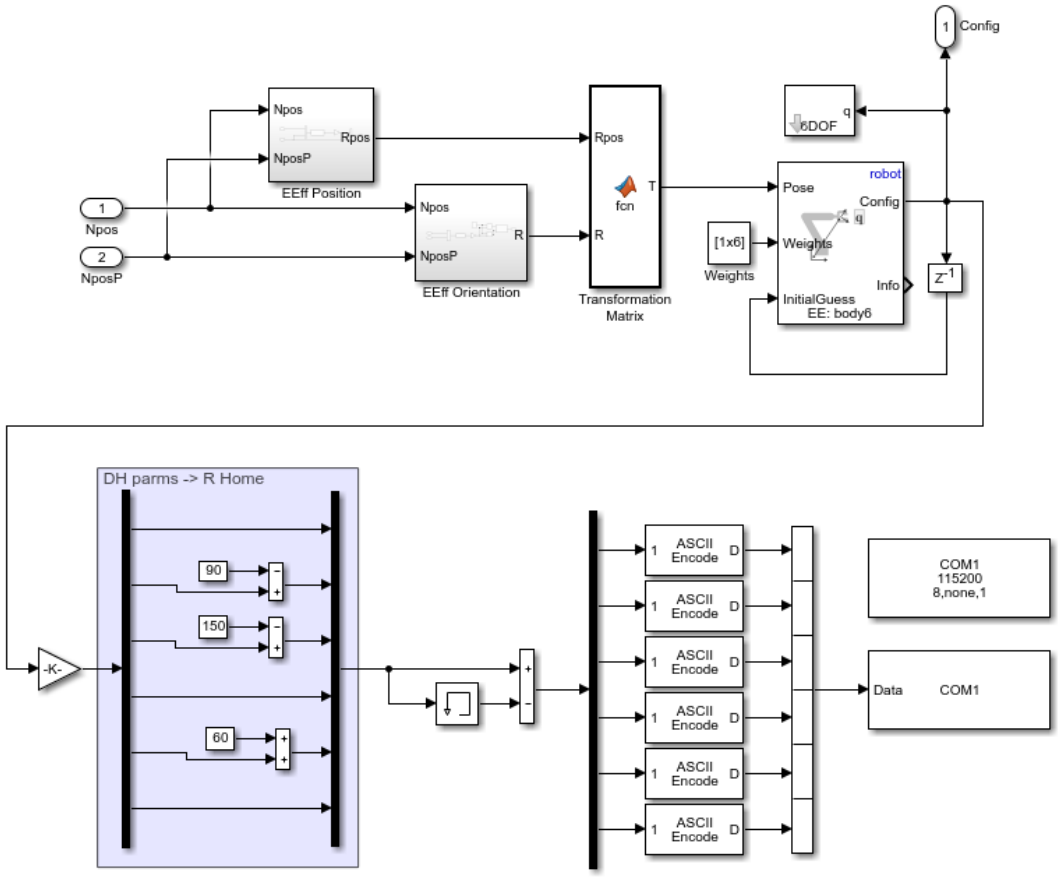

Figure 14 EEff Position & Orientation Subassembly: with inverse kinematics

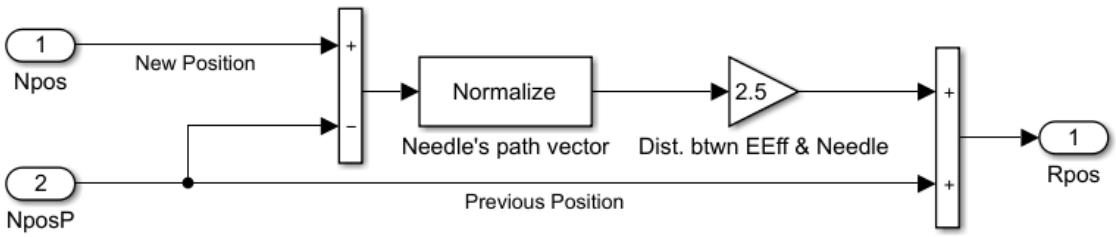

Figure 15 EEff Position Subassembly

The end effector magnet's magnetic field needs to be aligned with needle's magnetic field. This is how the orientation of the end effector is determined, by aligning its z-axis

with the direction that the needle is moving in. The series of equations below (Jur van den Berg, 2013) are used to calculate the rotation matrix for aligning the z-axis onto another axis, $\hat{n}$. Figure 16 shows the end effector orientation calculation.

$$v = \hat{z} \times \hat{n} \tag{6}$$

$$d = \hat{z} \cdot \hat{n} \tag{7}$$

$$[v]_\times \stackrel{\text{def}}{=} \begin{bmatrix} 0 & -v_3 & v_2 \\ v_3 & 0 & -v_1 \\ -v_2 & v_1 & 0 \end{bmatrix} \tag{8}$$

$$R = I + [v]_\times + [v]_\times^2 \cdot \frac{1}{1+d} \tag{9}$$

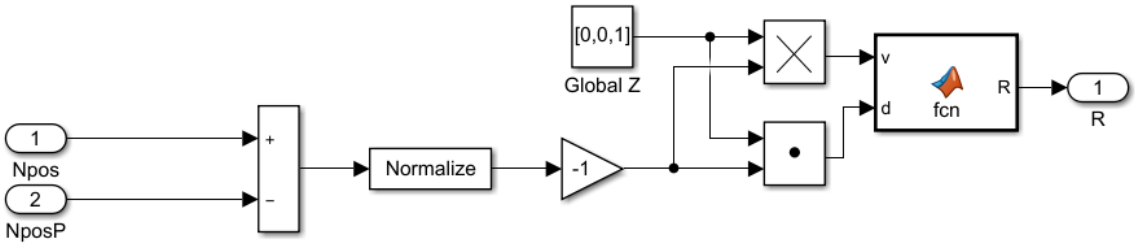

Figure 16 EEff Orientation Subassembly

A [4x4] transformation matrix is then inputted into the Robotics Systems Toolbox's inverse kinematics block (Figure 14). Equal weight was given to the end effector's desired position in x, y and z, as well as the orientation of the z-axis. No weight was given to the orientation of the x and y-axes as their orientation does not contribute to the direction of the needle. The output from the inverse kinematics block is a [6x1] vector of joint angles (radians), which are then plotted using Peter Corke's plot block. The vector is converted to degrees, then translated from the DH parameters to the physical robot's home position. This is a necessary step because θi=0 is a different position in the

Simulink model than what θi=0 is for each stepper motor. The Arduino code for sending steps to each motor does not keep a memory of the robot's previous position, therefore a memory is kept in Simulink. The memory is needed in order to send Arduino the number of degrees that each motor should move by. In the Simulink model, θ is a true position relative to the global frame; in Arduino θ is the difference between the previous position and the next position. There is no feedback being sent from the motors on the robotic arm, so visual feedback is used to make sure the joints move as desired.

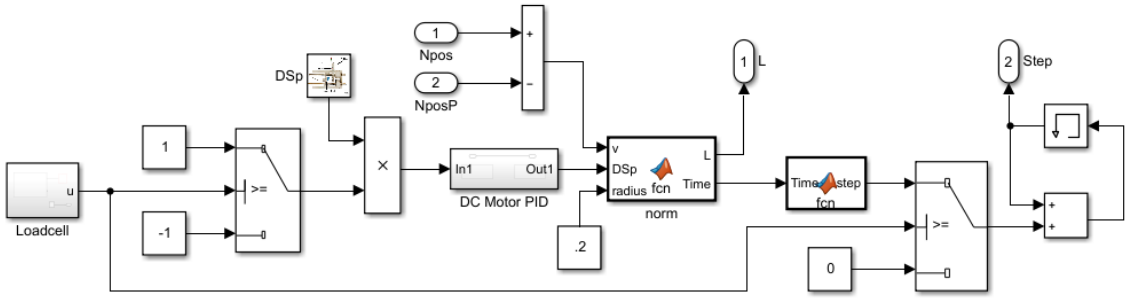

Figure 17 DC Motor Subassembly

The DC Motor subsystem from Figure 11 uses inputs Npos and NposP and outputs the length L that the needle travels from its previous position to its next. It also outputs Step which is an integer used to iterate through the columns of the [3xN] vector Npos from the workspace; it essentially tells the tracker to move the needle to its next position. Figure 17 shows a closer look at the DC Motor subsystem. The values from the loadcell are read from a National Instruments DAQ. When the loadcell reads values that are deemed as slack, the tracking system does not step forward and the DC motor's direction is reversed. A switch block is used in Simulink to forward a gain of 1 or -1 to multiply with the input DC motor speed, DSp. This value is sent to the Arduino Mega

that controls the DC motor speed. The Arduino code includes PID control and is included in the Appendix. The actual speed of the motor is sent to Simulink from the Arduino and is inputted into the MATLAB Function block labelled norm. The length L is equal to the norm of the vector between consecutive needle positions. The time it takes the needle to travel from its previous position to its new position is calculated in the MATLAB function block, labeled norm, and is calculated from the equation below, where r is the radius of the spindle that the Kevlar string is wrapped around.

$$Time = \frac{L}{DSp \cdot 2 \cdot \pi \cdot r} \tag{10}$$

If DSp is going in the reverse direction, where its sign is negative, the norm block will output a length and time of zero. The second MATLAB Function block has the following code:

```
function step = fcn(Time)
a = 0;
tic
while a<=Time
    a=toc;
end
step=1;
```

When the amount of time it takes the needle to move from one position to the next is reached, a single step is sent to the second switch block. If there is no slack in the string, the DC Motor subsystem will send an incremented step of 1 to the Npos subsystem. If there is slack, a 0 increment is sent, and the tracking system does not move on to the next position.

The last subsystem from Figure 11, Needle Position Prediction, takes inputs L and the [6x1] configuration of the robotic arm. A look inside the subsystem is shown in Figure 18.

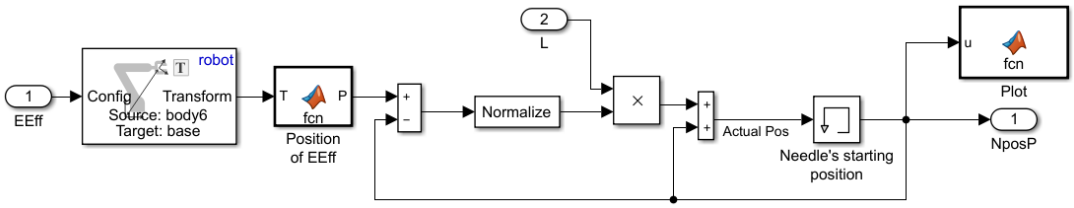

Figure 18 Needle Position Prediction Subassembly

For inverse kinematics, a desired end effector position and orientation are the input in the form of a transformation matrix and joint angles are the output. If the desired end effector pose is in the achievable workspace, inverse kinematics should accurately calculate the joint angles; the kinematics blocks from Robotics System Toolbox know the workspace of the robotic arm and determine joint angles within the workspace. The Inverse Kinematics block provided by Robotics Systems Toolbox has an input of a [1x6] vector of weights on the tolerance for orientation and position of the end effector for this reason. It also has an Info output that provides information about the associated error. To accurately calculate the position and orientation of the needle, the actual position of the end effector is needed. Ideally, there would be feedback from each of the joint motors, so that it would be known by how many degrees each motor physically rotates, but the robotic arm used in this project does not have that capability. If feedback could be received from the robotic arm, the actual position of the end effector could be found by using forward kinematics. Instead, forward kinematics is performed using the angles that are output from the inverse kinematics. At first it might seem redundant doing inverse kinematics and then forward kinematics when there is no feedback from the joints in the first place, but it can be a necessary step for testing new needle paths when there is little knowledge about the end effector path. Inverse kinematics solves for joint angles that may include some error, like for instances where

the desired transformation matrix is not in the robot's workspace. By doing forward kinematics on those joint angles, the end effector position can be more accurately estimated.

It is known that the needle will be moving along the vector between its previous position and the magnet located at the end effector. It is also known that the magnet will move a length L if there is no slack in the string. Combining this knowledge, the needle's position and orientation can be predicted. A memory block is used in Figure 17 so the needle's new position relative to its previous position can be found in the global frame. It is also in this memory block that the needle's starting position is defined.

3.2.5.1 Simulation

Each subsystem was tested independently to make sure they were running as expected. Once debugging was finished, two different paths were simulated: a straight line starting at (-12,0,5) with a constant z=5 (Figure 19); and a curved path with the following equation, where z is set to 5 and the starting position is (-12,0,5) (Figure 20). Figure 19 and Figure 20 show zoomed-in pictures of the robotic arm in order to show the path.

$$(x + 13.5)^2 + (y - 2)^2 = 2.5^2 \quad (11)$$

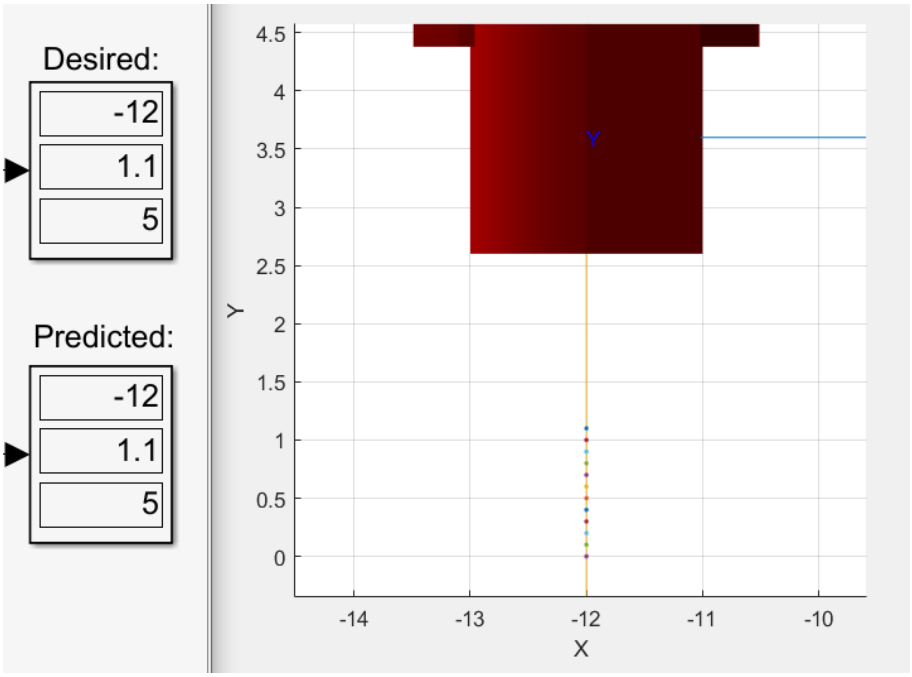

Figure 19 Simulation with a Straight Path: no error

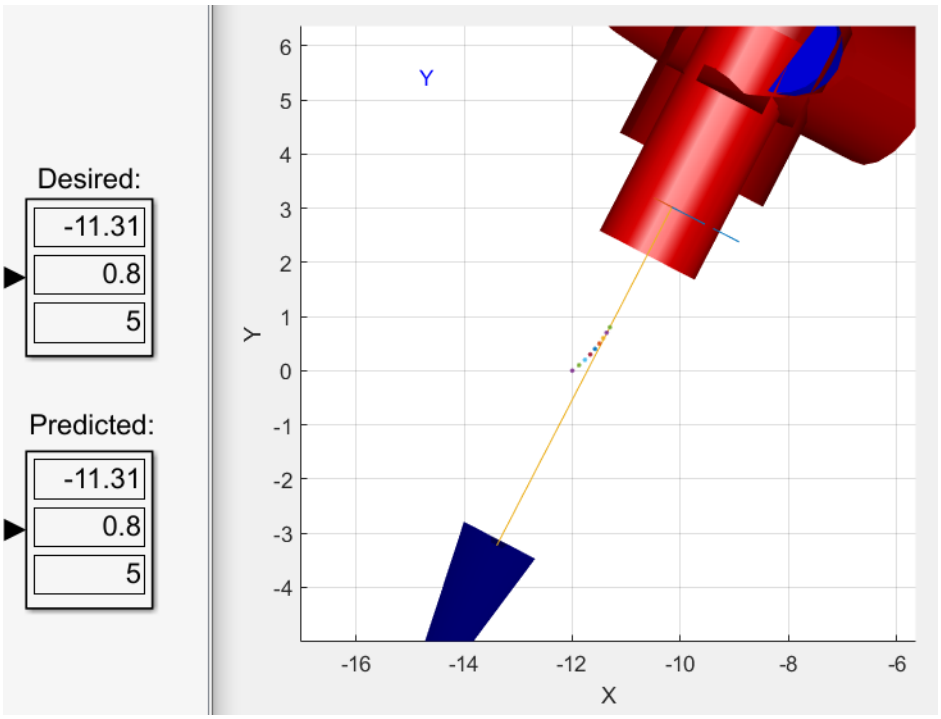

Figure 20 Simulation with a Circular Path: no error

3.4 Preliminary Experiments

While testing the complete system has yet to be initiated, testing individual components has proven to be successful. The DC motor PID control achieved minimal overshoot with a settling time of approximately 0.4 seconds. The loadcell values were also verified and tested alongside the rest of the loadcell/DC motor assembly; when the forces read from the loadcell changed, representing slack in the Kevlar, the DC motor switched directions and rewound the Kevlar as desired. In addition, to validate the puncturing force applied on the needle from the magnet, the needle, and the Kevlar tether attached to it, were successfully dragged through the gel with a single magnet by hand. From 2.5 inches away the needle was able to move in the direction of the magnet. When moving the magnet from side to side, while slowly releasing the tether, the needle was able to follow. Simulation also proved to be successful, showing that each component of the Simulink code can work together to track the needle in theory.

3.5 Future Work

This tracking system is merely a proof of concept, consequently more future work is required. The first concept addressed here is the magnet configuration. Several attempts were made to design a more improved configuration, similar to the work done in Zarrouk et al. (Zarrouk, Belharet, Tahri, & Ferreira, 2019). Having an enhanced magnet configuration can improve the control of the needle. With a single magnet, the needle experiences a single pulling force in the direction of the magnet. With a configuration including multiple permanent magnets, the needle would experience more forces from different directions, including torques, to re-stabilize the needle if it were to diverge from its desired path. Also, with a multi-magnet configuration, having a path within the reachable workspace of the end effector would be easier. For example, if the needle

needed to be steered in the abdomen but also needed to move cephalad (towards the head) along its path, the robotic arm would then have to move above the head to orient the needle in that direction. There are several problems with this action. First, the time it would take the arm to move back and forth from these positions would be too long, as the DC motor is unspooling thread at a constant speed. Second, it would be a safety concern. A very strong magnet would be required to generate force on the needle from a larger distance. Having a large force on an object within the body is dangerous if the needle broke from its Kevlar string, or the Kevlar could slice through frail tissue. It is also unsafe having many organs between the needle and magnet, in case the tether did somehow snap.

Other necessary future work is having an improved robotic arm with feedback and speed control over the joints. The needle's position relies heavily on the location of the end effector and a flaw with this tracking system is that the robotic arm relies on human visual feedback. This method does not guarantee that the end effector is moving to the desired position. For the robotic arm used in this project, the motors often slip and can very easily lead to the wrong calculation. Also, controlling the speed of the joints would provide better control on the location of the end effector.

An improved needle design is also necessary for future work. The needle designed in this thesis is merely for proof of concept. Instead of using a cylindrical magnet with a severed needle tip and Kevlar string, an ideal needle would have a machined magnetic needle tip and a non-elastic tube for which clinical drugs could travel through. Having a needle tip machined out of a magnet would help align the magnetic field with the sharp tip of the needle, improving the steerability of the needle. More research would have to be done as well to find a proper tube for the needle.

Lastly, experimentation must be done to test the system. To perform experiments, the issues with the current robotic arm and Arduino communication must be resolved. Then to test the accuracy, a clear gel with visual feedback would be used to determine if the tracking system is accurately predicting the position and orientation of the needle. Once there is data to analyze, finding ways in which to improve the system would be less challenging.

CHAPTER 4

CONCLUSION

The results from the tunable soft electronics show that there is standardized method for tuning these devices. The variability in inductance, capacitance and impedance prove that changing the position of the mobile component can alter the characteristic properties of each electrical unit. The characteristic properties changed by 20-23% for inductors, 12.7% for capacitors, and 185.3% for resistors. This project can hopefully be applied to advancing medical devices and improving the lives of many.

The most complicating assumption that the tracking system makes is that the needle will always move as expected with regards to where the large permanent magnet is located. If there are not enough controlling forces acting upon the needle, the needle may not always follow the path between its previous position and the magnet. In previous work from Ilami et al., when the needle diverged from its desired path, visual feedback was used to resolve the errors with high accuracy. However, the goal for this tracking system is to remove the necessity of visual feedback. The tracking system presented in this thesis uses feedback from the previous predicted needle position to determine the next location of the end effector, meaning, if the needle diverges from its desired path, the program will use the error to correct it. From the simulation, it appears that the program is working, however it is still necessary to run experiments. Without further experimentation, no conclusions can be drawn about the success of this tracking system.

REFERENCES

Abolhassani, N., Patel, R., & Moallem, M. (2007). Needle insertion into soft tissue: A survey. *Medical engineering & physics, 29*(4), 413-431.

Assadsangabi, B., Ali, M. M., & Takahata, K. (2012). Ferrofluid-based variable inductor. *Micro Electro Mechanical Systems (MEMS), 2012 IEEE 25th International Conference on*, (pp. 1121–1124).

Bae, Y. H., & Park, K. (2011). Targeted drug delivery to tumors: myths, reality and possibility. *Journal of controlled release, 153*(3), 198.

Barbone, A. S., Meftah, M., Markiewicz, K., & Dellimore, K. (2019). Beyond wearables and implantables: a scoping review of insertable medical devices. *Biomedical Physics & Engineering Express, 5*(6), 062002.

Benam, K. D., Talebi, H. A., & Khosravi, M. A. (2019). Full Order High Gain Observer Design for Image-Guided Robotic Flexible Needle Steering. *2019 27th Iranian Conference on Electrical Engineering (ICEE)* (pp. 1151-1156). IEEE.

Borduz, L., & Raj, K. (1987, 8). Low viscosity, electrically conductive ferrofluid composition and method of making and using same. *Low viscosity, electrically conductive ferrofluid composition and method of making and using same*. Google Patents.

Borwick, R. L., Stupar, P. A., DeNatale, J. F., Anderson, R., & Erlandson, R. (2003, 1). Variable MEMS capacitors implemented into RF filter systems. *IEEE Trans. Microwave Theory Tech., 51*, 315-319. doi:10.1109/TMTT.2002.806519

Buyantuev, B., Vorobev, E., Turgaliev, V., Kholodnyak, D., & Baskakova, A. (2018, 5). Electrically controlled variable inductors for applications in tunable filters. *2018 22nd International Microwave and Radar Conference (MIKON)*, (pp. 487-491). doi:10.23919/MIKON.2018.8405264

Cabreros, S. S., Jimenez, N. M., Greer, J. D., Adebar, T. K., & Okamura, A. M. (2015). Remote electromagnetic vibration of steerable needles for imaging in power Doppler ultrasound. *2015 IEEE International Conference on Robotics and Automation (ICRA)*, 2244-2249.

Carle, F., Bai, K., Casara, J., Vanderlick, K., & Brown, E. (2017). Development of magnetic liquid metal suspensions for magnetohydrodynamics. *Phys. Rev. Fluids, 2*, 013301.

Choi, W. M., Song, J., Khang, D.-Y., Jiang, H., Huang, Y. Y., & Rogers, J. A. (2007). Biaxially stretchable wavy silicon nanomembranes. *Nano Lett., 7*, 1655–1663.

Dickey, M. D. (2014). Emerging applications of liquid metals featuring surface oxides. *ACS Appl. Mater. Interfaces, 6*, 18369–18379.

Gray, D. S., Tien, J., & Chen, C. S. (2004). High-Conductivity Elastomeric Electronics. *Adv. Mater., 16*, 393-397. doi:10.1002/adma.200306107

Guerreiro, A. S., & Grotzer, M. (2018). Cerebellar tumors. *Handb. clinical neurology, 155*, 289-299.

Hartshorne, H., Backhouse, C. J., & Lee, W. E. (2004). Ferrofluid-based microchip pump and valve. *Sens. Actuators, B, 99*, 592–600.

Hiscocks, P. D. (2006). *Analog Electronic Circuit Design*. John Wiley & Sons, Incorporated. Retrieved from https://books.google.com/books?id=zK5ZAAAACAAJ

Hsu, Y.-Y., Gonzalez, M., Bossuyt, F., Vanfleteren, J., & De Wolf, I. (2011). Polyimide-enhanced stretchable interconnects: design, fabrication, and characterization. *IEEE Trans. Electron Devices, 58*, 2680–2688.

Ilami, M., Ahmed, R. J., Edwards, D., Thompson, E., Zeinolabedinzadeh, S., & Marvi, H. (2019). Magnetically Actuated Tunable Soft Electronics. ACS omega. Retrieved from https://pubs.acs.org/doi/10.1021/acsomega.9b02716

Ilami, M., Ahmed, R. J., Petras, A., Beigzadeh, B., & Marvi, H. (2020). Magnetic Needle Steering in Soft Phantom Tissue. *Scientific Reports, 10*(1), 1-11.

Ito, Y., Yoshihara, Y., Sugawara, H., Okada, K., & Masu, K. (2005, 11). A 1.3-2.8 GHz Wide Range CMOS LC-VCO Using Variable Inductor. *2005 IEEE Asian Solid-State Circuits Conference*, (pp. 265-268). doi:10.1109/ASSCC.2005.251716

James, J., Boys, J., & Covic, G. (2005, 11). A variable inductor based tuning method for ICPT pickups. *2005 International Power Engineering Conference*, (pp. 1142-1146 Vol. 2). doi:10.1109/IPEC.2005.207079

Jeon, J., Lee, J.-B., Chung, S. K., & Kim, D. (2017). On-demand magnetic manipulation of liquid metal in microfluidic channels for electrical switching applications. *Lab Chip, 17*, 128–133.

Jur van den Berg, (.-v.-d.-b. (2013, August 26). Calculate Rotation Matrix to align Vector A to Vector B in 3d? Mathematics Stack Exchange. Retrieved from https://math.stackexchange.com/q/476311

Kaltenbrunner, M., Kettlgruber, G., Siket, C., Schwödiauer, R., & Bauer, S. (2010). Arrays of ultracompliant electrochemical dry gel cells for stretchable electronics. *Adv. Mater., 22*, 2065–2067.

Khang, D.-Y., Jiang, H., Huang, Y., & Rogers, J. A. (2006). A stretchable form of single-crystal silicon for high-performance electronics on rubber substrates. *Science, 311*, 208–212.

Kim, D.-H., Song, J., Choi, W. M., Kim, H.-S., Kim, R.-H., Liu, Z., . . . Rogers, J. A. (2008). Materials and noncoplanar mesh designs for integrated circuits with linear elastic responses to extreme mechanical deformations. *Proc. Natl. Acad. Sci. U. S. A., 105*, 18675–18680.

Kim, D.-H., Xiao, J., Song, J., Huang, Y., & Rogers, J. A. (2010). Stretchable, Curvilinear Electronics Based on Inorganic Materials. *Adv. Mater., 22*, 2108-2124. doi:10.1002/adma.200902927

Kummer, M. P., Abbott, J. J., Kratochvil, B. E., Borer, R., Sengul, A., & Nelson, B. J. (2010). OctoMag: An electromagnetic system for 5-DOF wireless micromanipulation. *IEEE Transactions on Robotics, 26*(6), 1006-1017.

Lanzara, G., Salowitz, N., Guo, Z., & Chang, F.-K. (2010). A Spider-Web-Like Highly Expandable Sensor Network for Multifunctional Materials. *Adv. Mater., 22*, 4643–4648.

Lazarus, N., Meyer, C. D., Bedair, S. S., Nochetto, H., & Kierzewski, I. M. (2014). Multilayer liquid metal stretchable inductors. *Smart Mater. Struct., 23*, 085036.

Lewis, J. S., & Weaver, M. S. (2004). Thin-film permeation-barrier technology for flexible organic light-emitting devices. *IEEE J. Sel. Top. Quantum Electron., 10*, 45–57.

Liu, S., Sun, X., Hildreth, O. J., & Rykaczewski, K. (2015). Design and characterization of a single channel two-liquid capacitor and its application to hyperelastic strain sensing. *Lab Chip, 15*, 1376–1384.

Liu, Y., Pharr, M., & Salvatore, G. A. (2017). Lab-on-Skin: A Review of Flexible and Stretchable Electronics for Wearable Health Monitoring. *ACS Nano, 11*, 9614-9635. doi:10.1021/acsnano.7b04898

Love, L. J., Jansen, J. F., McKnight, T. E., Roh, Y., Phelps, T. J., Yeary, L. W., & Cunningham, G. T. (2005). Ferrofluid field induced flow for microfluidic applications. *IEEE/ASME Trans. Mechatronics, 10*, 68–76.

Lu, T., Wissman, J., & Majidi, C. (2015). Soft anisotropic conductors as electric vias for ga-based liquid metal circuits. *ACS Appl. Mater. Interfaces, 7*, 26923–26929.

Majidi, C. (2019, 12). Soft Matter Engineering for Soft Robotics. *Adv. Mater. Technol., 4*, 1800477. doi:10.1002/admt.201800477

Martel, S., Mathieu, J.-B., Felfoul, O., Chanu, A., Aboussouan, E., Tamaz, S., & Pouponneau. (2007). Automatic navigation of an untethered device in the artery of a living animal using a conventional clinical magnetic resonance imaging system. *Applied physics letters, 90*(11).

Mehta, R. V., Upadhyay, R. V., Dasannacharya, B. A., Goyal, P. S., & Rao, K. S. (1994). Magnetic properties of laboratory synthesized magnetic fluid and their temperature dependence. *J. Magn. Magn. Mater., 132*, 153–158.

Oh, D.-W., Jin, J. S., Choi, J. H., Kim, H.-Y., & Lee, J. S. (2007). A microfluidic chaotic mixer using ferrofluid. *J. Micromech. Microeng., 17*, 2077.

Oh, J. Y., Lee, D., & Hong, S. H. (2018). Ice-Templated Bimodal-Porous Silver Nanowire/PDMS Nanocomposites for Stretchable Conductor. *ACS Appl. Mater. Interfaces, 10*, 21666–21671.

Pamme, N. (2006). Magnetism and microfluidics. *Lab Chip, 6*(1), 24-38. doi:10.1039/B513005K

Pang, C., Lee, C., & Suh, K.-Y. (2013). Recent advances in flexible sensors for wearable and implantable devices. *J. Appl. Polym. Sci., 130*, 1429-1441. doi:10.1002/app.39461

Pant, R., Dhawan, S., Suri, D. K., Arora, M., Gupta, S. K., Koneracká, M., . . . Timko, M. (2004, 8). Synthesis and characterization of ferrofluid-conducting polymer composite. *Indian J. Eng. Mater. Sci., 11*, 267-270.

Park, S., Mondal, K., Treadway III, R. M., Kumar, V., Ma, S., Holbery, J. D., & Dickey, M. D. (2018). Silicones for stretchable and durable soft devices: Beyond Sylgard-184. *ACS Appl. Mater. Interfaces, 10*, 11261–11268.

Polcar, P., & Mayer, D. (2016). Magnetic Field Controlled Capacitor. *J. Electr. Eng., 67*, 227.

Reed, K. B., Okamura, A. M., & Cowan, N. J. (2009, May). Controlling a robotically steered needle in the presence of torsional friction. *IEEE International Conference on Robotics and Automation*, 3476-3481.

Rogers, J. A., Someya, T., & Huang, Y. (2010). Materials and Mechanics for Stretchable Electronics. *Science, 327*, 1603–1607. doi:10.1126/science.1182383

Rosset, S., Niklaus, M., Dubois, P., & Shea, H. R. (2009). Metal ion implantation for the fabrication of stretchable electrodes on elastomers. *Adv. Funct. Mater., 19*, 470–478.

Tan, S.-H., Nguyen, N.-T., Yobas, L., & Kang, T. G. (2010). Formation and manipulation of ferrofluid droplets at a microfluidic T-junction. *J. Micromech. Microeng., 20*, 045004.

Trung, T. Q., & Lee, N.-E. (2017). Recent Progress on Stretchable Electronic Devices with Intrinsically Stretchable Components. *Adv. Mater., 29*, 1603167. doi:10.1002/adma.201603167

Wagner, S., & Bauer, S. (2012, 3). Materials for stretchable electronics. *MRS Bulletin, 37*, 207–213. doi:10.1557/mrs.2012.37

Wang, C., Wang, C., Huang, Z., & Xu, S. (2018, 8). Materials and Structures toward Soft Electronics. *Adv. Mater., 30*, 1801368. doi:10.1002/adma.201801368

Wang, M. R., Trlica, C., Khan, M. R., Dickey, M. D., & Adams, J. J. (2015). A reconfigurable liquid metal antenna driven by electrochemically controlled capillarity. *J. Appl. Phys., 117*, 194901.

Wolfle, W. H., & Hurley, W. G. (2003, 1). Quasi-active power factor correction with a variable inductive filter: theory, design and practice. *IEEE Trans. Power Electron., 18*, 248-255. doi:10.1109/TPEL.2002.807135

Xia, Y., & Whitesides, G. M. (1998). Soft lithography. *Angew. Chem., Int. Ed., 37*, 550–575.

Yao, S., & Zhu, Y. (2015). Nanomaterial-Enabled Stretchable Conductors: Strategies, Materials and Devices. *Adv. Mater., 27*, 1480-1511. doi:10.1002/adma.201404446

Yao, S., Swetha, P., & Zhu, Y. (2018). Nanomaterial-Enabled Wearable Sensors for Healthcare. *Adv. Healthcare Mater., 7*, 1700889. doi:10.1002/adhm.201700889

Zarrouk, A., Belharet, K., Tahri, O., & Ferreira, A. (2019). A Four-magnet System for 2D Wireless Open-Loop Control of Microrobots. *2019 International Conference on Robotics and Automation (ICRA)*, (pp. 883–888).

Zeng, J., Deng, Y., Vedantam, P., Tzeng, T.-R., & Xuan, X. (2013). Magnetic separation of particles and cells in ferrofluid flow through a straight microchannel using two offset magnets. *J. Magn. Magn. Mater., 346*, 118–123.

Zou, J., Liu, C., Schutt-Aine, J., Chen, J., & Kang, S.-M. (2000, 12). Development of a wide tuning range MEMS tunable capacitor for wireless communication systems. *International Electron Devices Meeting 2000. Technical Digest. IEDM (Cat. No.00CH37138)*, (pp. 403-406). doi:10.1109/IEDM.2000.904341

APPENDIX A

MATLAB CODE FOR DEFINING ROBOTIC ARM IN PETER CORKE AND ROBOTICS SYSTEM TOOLBOX

```
clear
clc
addpath(genpath('rvctools'))
warning off

Npos=importdata('data2.txt');
nnn=length(Npos(:,1));
nn=nnn+1;
Nposx(2:nn)=Npos(:,1)';
Nposy(2:nn)=Npos(:,2)';
Nposz(2:nn)=Npos(:,3)';

qlim = [-pi 0.838 2.356 -2*pi -2.967 -2*pi;
        pi 3.927 4.538  2*pi  2.967  2*pi]';

robot = robotics.RigidBodyTree;
base = robot.BaseName;

body1 = robotics.RigidBody('body1');
jnt1 = robotics.Joint('jnt1','revolute');
body2 = robotics.RigidBody('body2');
jnt2 = robotics.Joint('jnt2','revolute');
body3 = robotics.RigidBody('body3');
jnt3 = robotics.Joint('jnt3','revolute');
body4 = robotics.RigidBody('body4');
jnt4 = robotics.Joint('jnt4','revolute');
body5 = robotics.RigidBody('body5');
jnt5 = robotics.Joint('jnt5','revolute');
body6 = robotics.RigidBody('body6');
jnt6 = robotics.Joint('jnt6','revolute');

%           a    alpha  d   theta
dhparams = [0     pi/2  6.66 0;
            8.7   0     0    0;
            0     pi/2  0    0;
            0    -pi/2  9.06 0;
            0     pi/2  0    0;
            0     0     3.78  0];

setFixedTransform(jnt1,dhparams(1,:),'dh');
setFixedTransform(jnt2,dhparams(2,:),'dh');
setFixedTransform(jnt3,dhparams(3,:),'dh');
setFixedTransform(jnt4,dhparams(4,:),'dh');
setFixedTransform(jnt5,dhparams(5,:),'dh');
setFixedTransform(jnt6,dhparams(6,:),'dh');

body1.Joint = jnt1;
body2.Joint = jnt2;
body3.Joint = jnt3;
body4.Joint = jnt4;
body5.Joint = jnt5;
body6.Joint = jnt6;
```

```
addBody(robot,body1,'base');
addBody(robot,body2,'body1');
addBody(robot,body3,'body2');
addBody(robot,body4,'body3');
addBody(robot,body5,'body4');
addBody(robot,body6,'body5');

robot.Bodies{1,1}.Joint.PositionLimits = qlim(1,:);
robot.Bodies{1,2}.Joint.PositionLimits = qlim(2,:);
robot.Bodies{1,3}.Joint.PositionLimits = qlim(3,:);
robot.Bodies{1,4}.Joint.PositionLimits = qlim(4,:);
robot.Bodies{1,5}.Joint.PositionLimits = qlim(5,:);
robot.Bodies{1,6}.Joint.PositionLimits = qlim(6,:);

L1 = 6.66; % link lengths
L2 = 8.7;
L3 = 5.18;
L4 = 3.88;
L5 = 1.78;
L6 = 2;

Link1 = Link('alpha',pi/2, 'a',0,  'd',L1,     'qlim',qlim(1,:));
Link2 = Link('alpha',0,    'a',L2, 'd',0,      'qlim',qlim(2,:));
Link3 = Link('alpha',pi/2, 'a',0,  'd',0,      'qlim',qlim(3,:));
Link4 = Link('alpha',-pi/2,'a',0,  'd',(L3+L4),'qlim',qlim(4,:));
Link5 = Link('alpha',pi/2, 'a',0,  'd',0,      'qlim',qlim(5,:));
Link6 = Link('alpha',0,    'a',0,  'd',(L5+L6),'qlim',qlim(6,:));

robot_pc = SerialLink([Link1 Link2 Link3 Link4 Link5 Link6],'name','6DOF');

alpha = timeseries(rand(2,1),'Name','alpha');
z = timeseries(rand(2,3),'Name','z');
```

Published with MATLAB® R2019b

APPENDIX B

ARDUINO CODE FOR CONTROLLING DC MOTOR

```
#define encoder0PinB 2
#define encoder0PinA 3
#define LOOPTIME 5
#define PWM_pin 10
#define direction_pin 9
unsigned long lastMilli = 0;
volatile long int encoder0Pos = 0;
unsigned int tmp_Pos = 1;
float speed_act = 0;
int speed_req = 1; //Tune the PID to reach that rpm
float Kp = 5;
float Kd = 0.5;
float Ki = 0;
boolean A_set;
boolean B_set;
int pid = 0;
int speed1 = 0;

void setup() {
  // put your setup code here, to run once:
  Serial.begin(9600);
  pinMode(direction_pin, OUTPUT);
  pinMode(encoder0PinA, INPUT);
  pinMode(encoder0PinB, INPUT);
  pinMode(PWM_pin, OUTPUT);
  // encoder pin on interrupt 0 (pin 2)
  attachInterrupt(0, doEncoderA, RISING);

  // encoder pin on interrupt 1 (pin 3)
  attachInterrupt(1, doEncoderB, RISING);
  //speed_req=Serial.parseInt();
  //Serial.println(speed_req);
  //analogWrite(PWM_pin,150);
}

void loop() {

  // put your main code here, to run repeatedly:

  if ((millis() - lastMilli) >= LOOPTIME) {
    lastMilli = millis();
    //getMotorSpeed();
    //speed_act = 1.25*1000/(millis() - lastMilli)* abs(encoder0Pos - countPrev);
    //countPrev = encoder0Pos;
    static long countPrev = 0;
    speed_act = (encoder0Pos - countPrev) * 1000 * 60 / (LOOPTIME * 720.989 * 12);
```

```
   //speed_act=(abs(encoder0Pos)-abs(countPrev))*1000*1.25/(LOOPTIME * 720.989);
   countPrev = encoder0Pos;
   pid = updatePid(pid, speed_req, speed_act);
   analogWrite(PWM_pin, pid);
   Serial.print(abs(int(speed_act * 100)));
   Serial.print("\n");
   //Serial.println(speed_act);
   //Serial.print(",");
   //Serial.println(encoder0Pos);
   //serial.println(encoder0Pos);
   if (Serial.available()) {
     speed_req = Serial.parseInt();
     if (speed_req < 6) {
       digitalWrite(direction_pin, HIGH);
     }
     else {
       digitalWrite(direction_pin, LOW);
       speed_req = speed_req - 6;
     }
   }
  }

}

//void getMotorSpeed()
//{
// static long countPrev=0;
//speed_act=(encoder0Pos-countPrev)*1000*1.25/(LOOPTIME * 720.989 *5);
//countPrev=encoder0Pos;
//}

int updatePid(int command, int targetValue, int currentValue)   {             // compute
PWM value
  float pidTerm = 0;                                                  // PID correction
  int error = 0;
  static int last_error = 0;
  static int errorsum = 0;
  error = abs(targetValue) - abs(currentValue);
  errorsum = errorsum + error;
  pidTerm = (Kp * error) + (Kd * (error - last_error) / LOOPTIME) + Ki * errorsum;
  //pidTerm = constrain(round(pidTerm),-2,2);
  last_error = error;
  return (command + int(pidTerm));
}

void doEncoderA() {
```

```
  // Low to High transition?
  if (digitalRead(encoder0PinA) == HIGH) {
    A_set = true;
    if (!B_set) {
      encoder0Pos = encoder0Pos + 1;

    }
  }

  // High-to-low transition?
  if (digitalRead(encoder0PinA) == LOW) {
    A_set = false;
  }

}


// Interrupt on B changing state
void doEncoderB() {

  // Low-to-high transition?
  if (digitalRead(encoder0PinB) == HIGH) {
    B_set = true;
    if (!A_set) {
      encoder0Pos = encoder0Pos - 1;
    }
  }
  // High-to-low transition?
  if (digitalRead(encoder0PinB) == LOW) {
    B_set = false;
  }
}
```

APPENDIX C

ARDUINO CODE FOR ROBOTIC ARM MOTOR ANGLES

The following code was written by Rohan Sharma, and Alagarasan Moorthi and is incomplete

```
// defines pins numbers
const int motor1 = 7; // changing steppin to motopins
const int dirPin1 = 33;
 const int motor2 = 8;
const int dirPin2 = 31;
 const int motor3 = 9;
const int dirPin3 = 29;
 const int motor4 = 10;
const int dirPin4 = 27;
const int motor5 = 11;
const int dirPin5 = 26;
const int motor6 = 12;
const int dirPin6 = 28;
int s[6] = {0,0,0,0,0,0};
int a[6];
int k[6] = {0,0,0,0,0,0};
int bb = 0;

int motor1forw(){
   digitalWrite(dirPin1,HIGH);
   digitalWrite(motor1,HIGH);
   delay(1);
   digitalWrite(motor1,LOW);
   delay(1);
}

int motor1back(){
   digitalWrite(dirPin1,LOW);
   digitalWrite(motor1,HIGH);
   delay(1);
   digitalWrite(motor1,LOW);
   delay(1);
}

int motor2forw(){
  digitalWrite(dirPin2,HIGH);
   digitalWrite(motor2,HIGH);
   delay(1);
   digitalWrite(motor2,LOW);
   delay(1);
}

int motor2back(){
```

```
  digitalWrite(dirPin2,LOW);
    digitalWrite(motor2,HIGH);
    delay(1);
    digitalWrite(motor2,LOW);
    delay(1);
}

int motor3forw(){
  digitalWrite(dirPin3,HIGH);
    digitalWrite(motor3,HIGH);
    delay(1);
    digitalWrite(motor3,LOW);
    delay(1);
}
int motor3back(){
  digitalWrite(dirPin3,LOW);
    digitalWrite(motor3,HIGH);
    delay(1);
    digitalWrite(motor3,LOW);
    delay(1);
}

int motor4forw(){
  digitalWrite(dirPin4,HIGH);
    digitalWrite(motor4,HIGH);
    delay(1);
    digitalWrite(motor4,LOW);
    delay(1);
}
int motor4back(){
  digitalWrite(dirPin4,LOW);
    digitalWrite(motor4,HIGH);
    delay(1);
    digitalWrite(motor4,LOW);
    delay(1);
}
int motor5forw(){
  digitalWrite(dirPin5,HIGH);
    digitalWrite(motor5,HIGH);
    delay(1);
    digitalWrite(motor5,LOW);
    delay(1);
}
int motor5back(){
  digitalWrite(dirPin5,LOW);
    digitalWrite(motor5,HIGH);
```

```
   delay(1);
   digitalWrite(motor5,LOW);
   delay(1);
}

int motor6forw(){
   digitalWrite(dirPin6,HIGH);
   digitalWrite(motor6,HIGH);
   delay(1);
   digitalWrite(motor6,LOW);
   delay(1);
}

int motor6back(){
   digitalWrite(dirPin6,LOW);
   digitalWrite(motor6,HIGH);
   delay(1);
   digitalWrite(motor6,LOW);
   delay(1);
}

void setup() {
  // Sets the two pins as Outputs
  pinMode(motor1,OUTPUT);
  pinMode(dirPin1,OUTPUT);
  pinMode(motor2,OUTPUT);
  pinMode(dirPin2,OUTPUT);
  pinMode(motor3,OUTPUT);
  pinMode(dirPin3,OUTPUT);
  pinMode(motor4,OUTPUT);
  pinMode(dirPin4,OUTPUT);
  pinMode(motor5,OUTPUT);
  pinMode(dirPin5,OUTPUT);
  pinMode(motor6,OUTPUT);
  pinMode(dirPin6,OUTPUT);
  Serial.begin(115200);

}
void loop() {
if (Serial.available()>0)
{
  for(int i=0;i<6;i++){
    k[i]= Serial.parseInt();
  }
}
//Serial.println(k[1]);
```

```
//int    k[6] = {Serial.parseInt()};
//int    k[6] = {0,0,30,20,10,100};


//Serial.println(bb);
a[0]=map(k[0],-360,360,-1600,1600);
a[1]=map(k[1],-360,360,-6780,6780);
a[2]=map(k[2],-360,360,-1600,1600);
a[3]=map(k[3],-360,360,-34500,34500);
a[4]=map(k[4],-360,360,-8100,8100);
a[5]=map(k[5],-360,360,-16000,16000);

if (a[0]>0 && s[0]<a[0])
{
  digitalWrite(dirPin1,HIGH);
    digitalWrite(motor1,HIGH);
    delay(1);
    digitalWrite(motor1,LOW);
    delay(1);
  s[0]=s[0]+1;
 //Serial.println(a[0]);

}
else if (a[0]<0 && s[0]<abs(a[0]))
{ motor1back();
 s[0]=s[0]+1;
}

if (a[1]>0 && s[1]<a[1])
{
  motor2forw();
  s[1]=s[1]+1;
}
else if (a[1]<0 && s[1]<abs(a[1]))
{ motor2back();
 s[1]=s[1]+1;

}

if (a[2]>0 && s[2]<a[2])
{
  motor3forw();
  s[2]=s[2]+1;
}
else if (a[2]<0 && s[2]<abs(a[2]))
```

```
{ motor3back();
 s[2]=s[2]+1;

}

if (a[3]>0 && s[3]<a[3])
{
  motor4forw();
  s[3]=s[3]+1;
}
else if (a[3]<0 && s[3]<abs(a[3]))
{ motor4back();
 s[3]=s[3]+1;

}

if (a[4]>0 && s[4]<a[4])
{
  motor5forw();
  s[4]=s[4]+1;
}
else if (a[4]<0 && s[4]<abs(a[4]))
{ motor5back();
 s[4]=s[4]+1;

}

if (a[5]>0 && s[5]<a[5])
{
  motor6forw();
  s[5]=s[5]+1;
  Serial.println(s[5]);
}
else if (a[5]<0 && s[5]<abs(a[5]))
{ motor6back();
 s[5]=s[5]+1;

}
```

APPENDIX D

COAUTHOR APPROVAL FOR ACS OMEGA PAPER

I have received approval from the coauthors on Magnetically Actuated Tunable Soft Electronics to use this publication in my thesis. The modifications that have been made to the paper were small grammar fixes and minor retitling of figures.